POLYTECHNIQUE MONTRÉAL
affiliée à l'Université de Montréal

High-sensitivity field resolved detection for terahertz time domain spectroscopy

BÉDI GRÉGORY-SAMUEL ZAGBAYOU
Département de génie physique

Mémoire présenté en vue de l'obtention du diplôme de *Maîtrise ès sciences appliquées*
Génie physique

Mai 2023

© Bédi Grégory-Samuel Zagbayou, 2023.

POLYTECHNIQUE MONTRÉAL
affiliée à l'Université de Montréal

Ce mémoire intitulé :

High-sensitivity field resolved detection for terahertz time domain spectroscopy

présenté par **Bédi Grégory-Samuel ZAGBAYOU**
en vue de l'obtention du diplôme de *Maîtrise ès sciences appliquées*
a été dûment accepté par le jury d'examen constitué de :

Stephan REUTER, président
Denis SELETSKIY, membre et directeur de recherche
Tsuneyuki OZAKI, membre externe

DEDICATION

To my friends and family,

ACKNOWLEDGEMENTS

I would like to thank Denis Seletskiy for making me a member of the femtoQ laboratory and his thoughtful supervision during my time here. He gave me the initial motivation to switch to a research oriented graduate program and his guidance continues to give me confidence, in my skills as well as my academic choice, in a great environment. I am also grateful to Stéphane Virally, for being available whenever we needed and always suggesting creative ways of getting stuff done.

I would also like to thank my femtoQ colleagues Patrick, Gabriel, Etienne, Laurent, Marco, Justine, Etienne, Emile, Sho, Shilong, Amin, Alexandre, as well as the interns Paul, Clarence-Olivier, Pavel, and Julien that give life to the laboratory. I would like to particularly thank Etienne, whose work I inherited and taught me everything I needed to know about my project. The quality of his work made mine easy. I would also like to thank Patrick, Etienne, Laurent and Gabriel, senior members that contributed, and continue to contribute to code without which this work would have been much harder. I would like to thank Marco and Clarence-Olivier, I spent the most time with them in the lab, and their questions and experience contributed vastly to my understanding of what I was doing.

I would like to thank Prof. Frédéric Sirois, whose electrical engineering expertise was crucial to this project, and for Clarence-Olivier's contribution in designing and manufacturing the Helmholtz coil.

Words cannot express how grateful I am for my friends, my family and my partner Nafha. Their patience with me is an infinite blessing and every moment spent with them gave me strength.

I am grateful to the technical staff, in particular Emile and Yves, who helped me fix various specific issues that I encountered with my set-up, and for their advice. I am also grateful for the department's administrative staff, for their support and patience.

The figures in this thesis have been made with inkscape, and I am grateful for the CompononentLibrary package that Alexander Franzen created.

RÉSUMÉ

Le "gap terahertz" constitue un espace entre les fréquences optiques et électroniques où il y avait peu de technologies développées par le passé. La spectroscopie des états fondamentaux de la matière, ainsi que des nouvelles possibilités technologiques pour la télécommunication, la sécurité et la santé ont motivé l'exploitation de techniques optiques ultrarapides pour couvrir cette section du spectre électromagnétique au cours des trente dernières années.

L'échantillonnage électro-optique et la rectification optique sont deux méthodes populaires de détection et de génération, respectivement, d'ondes terahertz. Elles sont employées pour réaliser de la spectroscopie terahertz dans le temps. La rectification optique est cependant délicate à implémenter et a des limites de performances évidentes. Ces deux points sont corrigés par les émetteurs spintroniques, un nouvel outil de génération d'ondes terahertz.

Dans ce projet, on améliore la sensibilité de la détection d'un dispositif spectroscopique, en exploitant la dépendance de la polarisation du champ térahertz produit par un émetteur spintronique sur l'orientation du champ magnétique dans lequel il est plongé.

Pour ce faire, nous avons d'abord identifié la meilleure fréquence à laquelle moduler le champ magnétique, en caractérisant le bruit relatif en intensité du laser source dans le domaine fréquentiel. Nous avons ainsi prévu une réduction du bruit d'un facteur de 40, en passant d'une émission de THz modulée à 200Hz à une modulation à plus de 160kHz. À ces fréquences de modulation, la sensibilité de la détection est à la limite classique standard pour notre laser.

Nous avons ensuite conçu une bobine Helmholtz avec un circuit doublement résonant, qui émet un champ magnétique sinusoïdal dans le temps, à une fréquence de 787kHz. Des mesures de la sensibilité ont été effectuées qui confirment nos estimations.

Nous avons par la suite réalisé des mesures de détection par échantillonnage électro-optique, en utilisant un émetteur spintronique plongé dans le champ de notre bobine pour générer les ondes térahertz. Les résultats démontrent que les performances sont similaires aux mesures faites à basse fréquence de modulation. Nous avons ainsi démontré que les émetteurs spintroniques fonctionnent à des fréquences avoisinant les fréquences radio. Nous faisons aussi par là une mesure totale de la bande d'émission de l'émetteur spintronique, qui s'étend jusqu'à 32THz à la ligne de 10%.

Nous avons enfin utilisé des mesures du champ émis par l'émetteur spintronique pour déduire le temps caractéristique de la diffusion électron-spin, qui est de l'ordre de 100 femtosecondes, comme trouvé dans la littérature.

ABSTRACT

The "terahertz gap" is the range between mid-infrared optical frequencies and electronic frequencies where few technologies were developed in the past. Spectroscopy of the fundamental states of matter, as well as new possibilities for telecommunication, security and health technology have prompted the use of ultrafast optical techniques to bridge that gap.

Electro-optic sampling and optical rectificaion are two popular methods used for detection and generation, respectively, of terahertz radiation. They are harnessed together for time-domain terahertz spectroscopy. Optical rectification is, however, difficult to implement and has limitations in its performance. Spintronic emitters are a novel and easier way of generating terahertz radiation that overcome the limitations of optical rectification.

In this project, we exploit the polarization dependency of spintronic emitted terahertz on the external magnetic field to drastically improve sensitivity.

To do so, we first characterise the relative intensity noise of laser source in the frequency domain. We find that for frequencies above 160kHz, the noise is at the standard quantum limit, which means a factor of 40 for the improvement of sensitivity by going from modulation at low frequency (200Hz) to modulation at near radio frequency.

We then design and build a Helmholtz coil with a double-resonant circuit. It emits a magnetic field, sinusoidal in time, at 787kHz. With this coil, noise measurements have been done, showing nearly a 40 times improvement when compared to modulation at 200Hz, and giving shot-noise limited sensitivity to our set-up.

Then, electro-optic sampling measurements were realised with the spintronic emitter as the source of terahertz radiation. The detected field proved to have the same features, whether modulated at 787kHz or at 200Hz, demonstrating full functionality for a spintronic emitter operating at near radio frequencies. We also detected a full bandwidth of 32THz at the 10% line, which constitutes the widest bandwidth in a measurement of spintronic emission to the date of this writing.

Finally, we used the detected spectrum from the spintronic emission to retrieve the time constant associated with the electron spin relaxation in the ferromagnetic layer. The results are in strong agreement with the literature.

TABLE OF CONTENTS

DEDICATION iii

ACKNOWLEDGEMENTS iv

RÉSUMÉ v

ABSTRACT vi

TABLE OF CONTENTS vii

LIST OF TABLES ix

LIST OF FIGURES x

LIST OF SYMBOLS AND ACRONYMS xiii

LIST OF APPENDICES xiv

CHAPTER 1 INTRODUCTION 1

1.1 General introduction 1

1.2 Research objectives 2

1.3 Thesis Outline 3

CHAPTER 2 THEORY 4

2.1 Terahertz generation and detection in nonlinear media 5

2.1.1 Optical rectification and electro-optic sampling in $\chi^{(2)}$ media 5

2.1.2 Phase matching 10

2.1.3 Distortion in an EOS set-up 13

2.2 Spintronic emission of terahertz radiation 14

2.3 Relative intensity noise 20

2.4 Theory of electronic methods 23

2.4.1 Lock-in detection 23

2.4.2 Boxcar averager 26

2.4.3 Double resonant circuit 27

2.5 Literature review 29

CHAPTER 3 RELATIVE INTENSITY NOISE CHARACTERIZATION 34
3.1 Ti:Sapphire RIN performance 34
3.1.1 Laser system 34
3.1.2 Noise characterization set-up 35
3.1.3 RIN performance and improvement benchmark 36
3.2 Negative delay electrooptic readout 42
3.2.1 EOS noise characterization set-up 42
3.2.2 Noise performance 44

CHAPTER 4 HIGH-SENSITIVITY FIELD RESOLVED MEASUREMENTS 48
4.1 Electro-optic sampling set-up 48
4.2 Low frequency measurements 50
4.3 High frequency measurements 54
4.3.1 Electron mobility analysis 56

CHAPTER 5 CONCLUSION 59
5.1 Summary of current works 59
5.2 Future work 60

REFERENCES 62

APPENDICES 68

LIST OF TABLES

Table 4.1 Noise performance with different optical filters in the ellipsometric set-up 53

LIST OF FIGURES

Figure 2.1 $\chi^{(2)}$ phenomena energy-level diagrams. **From left to right :** Sum-frequency generation, difference frequency generation, second harmonic generation, optical rectification. 7

Figure 2.2 Efficiency of SFG in phase-matched and non-phase matched configurations. 12

Figure 2.3 Schematic of the spintronic emitter. F: ferromagnetic layer, NF: non ferromagnetic layer, j_s: spin current, j_c: electrical current. 15

Figure 2.4 Schematic of the three temperature model. T_e: electron temperature, T_s: spin temperature, T_l: phonon temperature. 16

Figure 2.5 (a) Schematic of the band diagram in the F layer. The Fermi level for each spin state is shown, with passage from one to the other mediated by spin flips (white arrow). (b) Schematic of the electron-phonon scattering inducing the spin flip. 17

Figure 2.6 Time domain visualization of the effect of the lock-in amplifier. **Left :** Initial signal and reference, with different phases and amplitudes. **Right :** Signal after mixing with double frequency component and non zero mean. Filtered output takes out the higher frequency component. 24

Figure 2.7 Frequency domain representation of demodulation. **Left :** Initial signal and reference fed to the lock-in. **Right :** Mixing "displaces" the signal, while increasing orders of the same RC filter block out more noise. . . 25

Figure 2.8 Representation of the boxcar basic principle. **Top :** Input signal and boxcar train. **Bottom :** Cleaned signal and integrated value within each boxcar window. 26

Figure 2.9 Schematic of the double resonant circuit. L: inductance, C_s: series capacitance, C_p: parallel capacitance, R: resistance 27

Figure 3.1 Spectral output from the mode-locked Ti:Sa laser source. 35

Figure 3.2 Relative intensity noise characterisation optical set-up. The photodiode is connected to the boxcar system. 36

Figure 3.3 Time domain representation of the boxcar output. **Top :** Unfiltered. **Bottom :** 80Hz electrical high-pass filter applied to the output. . . . 37

Figure 3.4 Distribution of the boxcar output around the mean value with different averaging bandwidths. Gaussian fit done on the first histogram for reference. **Top :** Unfiltered output. **Bottom :** 80Hz electrical high-pass filter applied to the output. 38
Figure 3.5 Power spectral density (PSD) of the unfiltered Ti:Sa output, from 100Hz to 1MHz. The "plateau" reached at high frequencies is "carried" by the resolution limit of the experiment. 40
Figure 3.6 PSD of the photodiode and the Ti:Sa, with and without a 80Hz filter applied. The resolution floor is lowered by the filter, revealing features invisible in the unfiltered case, and reaching the shot-noise limited plateau at high frequencies. 40
Figure 3.7 PSD of the filtered Ti:Sa and the photodiode outputs, showing the two modulation frequencies targeted in the text. This work uses two common modulation frequencies (see section 4) at 200 Hz and 787kHz, shown by respective vertical lines for reference. 41
Figure 3.8 Picture of the prototype double resonant Helmholtz coil. 43
Figure 3.9 Distribution of the electro-optic(EO) readout at negative delay with the spintronic emitter in place. The inset "zooms" in on the distribution for near radio-frequency modulation. 45
Figure 3.10 Distribution of the electro-optic(EO) readout when the pump arm is blocked. The inset "zooms" in on the distribution for near radio-frequency modulation. 46
Figure 3.11 Distribution of the electro-optic(EO) readout at negative delay with the spintronic emitter in place, with a modulation frequency of 787kHz. The peak-to-peak voltage indicated is the one used to drive the coil. The dashed lines show a Gaussian fit to the different histograms. . . . 46
Figure 4.1 Schematic of the electrooptic sampling optical set-up. The two dashed rectangles without filling are the position for the coil (overlapping with GX) or optical chopper (empty rectangle). P: periscope. BS: 96/4 Beamsplitter. FS: 12mm thick Fused Silica. EOM: elasto-optic modulator. OAPM: Off Axis Parabolic Mirror (silver or gold coated). GX: Generation crystal. EOX: Electrooptic crystal. L: lens. OF: Optical filter. WP: Wollaston Prism. BPD: Balanced Photodiode 49

Figure 4.2 Comparison between the spintronic emitted THz, detected through 500μm thick ZnTe at different modulation frequencies. **Left :** Time traces. **Right :** Associated spectra. The dashed area is below the noise floor of the high-frequency modulated spectrum. 51

Figure 4.3 Comparison between the spintronic emitted THz, detected through 500μm thick ZnTe, at a modulation frequency of 787kHz for different optical filters in the ellipsometric set-up. **Left :** Time traces. **Right :** Associated spectra and phases. 53

Figure 4.4 Comparison between the spintronic emitted THz, detected through 30μm thick GaSe at different modulation frequencies. **Left :** Time traces. **Right :** Associated spectra. The dashed area is below the noise floor of the high-frequency modulated spectrum. 54

Figure 4.5 THz emission from the spintronic emitter, retrieved through deconvolution. **Left :** The detected spectra and phase are shown with the deconvoluted emission and phase, to which a Hanning window has been applied for apodisation. **Right :** The retrieved field, its Hilbert transform and their envelope in the time domain. 57

Figure 4.6 Fitting of the tail of the retrieved envelope of the spintronic emission, corrected by the response function of the EOS detector, and the associated lifetime. 58

LIST OF SYMBOLS AND ACRONYMS

DFG Difference frequency generation

DC Direct current

EOS Electro-optic Sampling

fs femtosecond

F Ferromagnetic

FWHM Full width half maximum

GaSe Gallium Selenide

GX Generation Crystal

EOX Electro-optic crystal

IR Infrared

MIR Mid-Infrared

Nd:YAG Neodymium-doped yttrium aluminum garnet

N Non ferromagnetic

OR Optical Rectification

ps picosecond

Si Silicon

SiC Silicon Carbide

SBR Signal to Background Ratio

SNR Signal to Noise Ratio

SFG Sum frequency generation

SHG Second harmonic generation

THz Terahertz

ZnTe Zinc Telluride

LIST OF APPENDICES

Appendix A Manufacturing of coil 68

CHAPTER 1 INTRODUCTION

1.1 General introduction

Traditionally, the "terahertz band" is defined as the section of the electromagnetic spectrum ranging from 0.1 Terahertz (THz) to 10THz [1–3]. During the development of technologies covering the bordering microwave and infrared (IR) range, the THz was of little interest due to the difficulty of access. Now that those nearing bands have mature techniques and instruments, the benefits of accessing the THz range are clearer and this work contributes to the last three decades of research done to bridge this gap.

On the microwave end, the finite speed of electronic oscillations required for high speed devices made the THz range unreachable. On the other hand, traditional IR sources have hardly been able to reach below 30THz. Further, IR tools have not proven suitable for long range communication due to absorption of common materials in the low THz region [4]. This section of the spectrum has justifiably been called the "fingerprint" range due to the specificity of the observed absorption lines. This fingerprint range, due to low energy vibration modes in materials, is then a great incentive for static THz spectroscopy. The low energy involved with THz radiation, coupled with the strong absorption in water, would also mean non-destructive probing tools, useful for remote security probing [5]. In that sense, spectroscopy was already a sufficient motivation for the THz quest. Because the frequencies involved are much higher than the electronic upper limits, THz radiation also opened the door for faster communication speed, especially over short distances, where it is seen as crucial for 6G, as demonstrated by recent advances in multiplexer technology [6].

While the mentioned applications of THz photonics show direct impact on every day human activity, there is in parallel an ongoing research, aimed to deepen our fundamental understanding of nature. Research concerns improvements in sources and detectors of THz radiation, in turn designed to improve existing and enable new spectroscopy modalities toward better understanding of light matter interaction at these photon energies. Unlike traditional photon-based detectors as in IR photonics, THz detectors enable tracing the evolution of the electric component of the electromagnetic radiation directly in time. As a result, this also enables traceability of the phase, important in more information-rich measurements of matter response to light. As such, THz tools are ready made for coherent optical control, which is required for new quantum technologies, but also for testing current quantum theory [7]. THz frequencies are high enough to be applicable toward interesting time-resolved spectroscopies, yielding insights into many low-energy excitations in solids, such as collective

electronic, spin, vibrational and other degrees of freedom. To improve these fundamental studies, much research is focused on the improving of THz technology, concentrated around searches and engineering approaches of better sources and detectors.

The last decades have seen many sources for THz radiation come to prominence. The free electron laser is a powerful source for pulsed THz radiation at low frequencies, while THz quantum cascade lasers offer similar power at higher frequencies for a continuous operation [8, 9]. These laser sources have yet to match the popularity of photoconductive antennas (PCA) and optical rectification (OR) for THz generation. These two techniques rely on ultrafast pulsed sources emitting in a more accessible frequency region, e.g. near-infrared, which are nowadays commonplace. PCA requires a biased semiconductor antenna, while the OR exploits non-linear optical responses from specific materials. These effects, along with the duration of the exciting pulse determine the bandwidth of the generated THz. Both techniques of PCA and OR can be reversed, in this case yielding PCA-based THz detector as well as electro-optic sampling (EOS) method. For pulsed THz, both detection methods rely on gating pulses. The short duration of the pulse, down to 10 femtoseconds (fs) for the common titanium sapphire laser, make them excellent probes for THz radiation with duration as low as 20fs, for a 10fs probe, and reaching up to a few picoseconds (ps). These sources tend to have high repetition rates (up to hundreds of megahertz), making them excellent candidates for fast modulation and high sensitivity measurements.

Another emerging method or THz generation relies on a spintronic effect in metallic thin-films. Similarly to PCA-based emitters, spintronic emitter requires an application of an external magnetic field, enabling conversion of an ultrashort pulse into a coherent THz radiation through the process of inverse spin-Hall effect and making them prime candidates for fast modulation. Combined with current EOS, it offers the possibility of coherent generation and detection of THz over a range three times larger than the considered THz range, with a sensitivity as low as the standard quantum limit (SQL). The highest sensitivity of any semi-classical metrology is bounded by the shot-noise of the source, yielding the SQL in detection. In turn, sensing beyond SQL would require non-classical sources and detectors. As such, demonstration of SQL-limited performance of any emitter or detector is not only the best metric for classical spectroscopy but shows the potential, in this case of spintronic emitter sources, for potential exploration toward the non-classical regime.

1.2 Research objectives

The project is aimed at optimizing the performance of THz emission from spintronic emitters. The emitter devices are obtained through an existing collaboration of the laboratory with

the researchers at the Freie Universität in Berlin. From the various quantities that can be improved, our goal is to device an easy to implement method to reduce the noise to a fundamental limit in a pump-probe set-up suited for spectroscopy. Toward this and contrary to traditional application of a static magnetic field, in this work we investigate subjecting spintronic emitters to a time-varying magnetic field, and study possible improvements in sensitivity. What modulation frequency is required for measurements at the SQL in our current set-up? How can we achieve magnetic field switching at such frequencies, given the constraint imposed by the current set-up? Does the spintronic emitter function at such frequencies? The first question is answered by experiments and data processing. The second question is answered by the design of an suitable electronic device, informed by calculation. The final question is answered by another set of experiments, and comparison of the processed data to existing values in the literature and from the set-up in another configuration.

1.3 Thesis Outline

The thesis is developed over three central chapters. The first one (chapter 2) contains a theoretical and phenomenological framework for the generation and detection of THz focused on OR, spintronic emission and EOS. It also contains the theory for the electronic methods required to achieve high-sensitivity detection, presented after a description of relative intensity noise (RIN). The chapter ends with a historical overview of THz detection by the main methods, and how noise performance improved along the way. The next chapter (chapter 3) treats with RIN in the EOS set-up, starting with the Ti:Sa source. The RIN then motivates the choice for the high modulation frequency of the magnetic field modulation method for the spintronic emitter. The comparison between measured noise at the initial frequency and at high frequency is presented and discussed afterwards. The last chapter (chapter 4) presents the measurement done with the spintronic emitter in low and high THz bandwidth schemes. There an assessment of the functioning of the spintronic emitter at such modulation frequencies for the magnetic field is done. Finally, literature values for the spin-electron relaxation time are confirmed through analysis of the measurements.

CHAPTER 2 THEORY

Generation and detection of radiation is accomplished through rigorous manipulation of light-matter interactions. In order to achieve such control, the interactions have to be carefully selected, carried out and registered. Thus, a fundamental understanding of the phenomena, as well as the devices used to carry out the interactions and register them is needed. This chapter introduces the theoretical and phenomenological frame required to understand and exploit them, discussed the key electronic devices used and their principles and ends by presenting a snapshot of the literature.

At the fundamental level, light-matter interactions are mediated by the Maxwell equations [10]:

$$\begin{aligned} \nabla \cdot \mathbf{D} &= \rho \\ \nabla \cdot \mathbf{B} &= 0 \\ \nabla \times \mathbf{E} &= -\frac{\partial \mathbf{B}}{\partial t} \\ \nabla \times \mathbf{H} &= \frac{\partial \mathbf{D}}{\partial t} + \mathbf{J} \end{aligned} \tag{2.1}$$

given here for the international system of units. In these equations, the free charges in space are represented by ρ while free currents are represented by $\mathbf{J}$. $\mathbf{H}$ and $\mathbf{D}$ represent the magnetizing and electric displacement field. These fields reduce respectively to $\mathbf{B}$ and $\mathbf{E}$ in vacuum, being linked to them through:

$$\begin{aligned} \mathbf{B} &= \mu_0(\mathbf{H} + \mathbf{M}) \\ \mathbf{D} &= \epsilon_0 \mathbf{E} + \mathbf{P} \end{aligned} \tag{2.2}$$

where $\mathbf{M}$ is the magnetization of the system under study, and P its polarization. Throughout this text, special care will be first be paid to understanding non-magnetic materials before discussing magnetic materials in the context of spintronic emitters. Because we are invested in the results of light-matter interactions, the charges under consideration are initially bound (ρ=0) and there is no free current ($\mathbf{J} = 0$). In this context, we can rewrite the Maxwell equations by taking the curl of the 3rd equation, substitute in 4th to arrive at the following equation:

$$\nabla \times \nabla \times \mathbf{E} + \frac{1}{c^2}\frac{\partial^2}{\partial t^2}\mathbf{E} = -\frac{1}{\epsilon_0 c^2}\frac{\partial^2 \mathbf{P}}{\partial t^2} \tag{2.3}$$

where $c = 1/\sqrt{\mu_0 \epsilon_0}$ is the speed of light in vacuum. In the case of transverse and infinite

plane waves, as considered in this text, the first term on the left can be reduced to a negative spatial laplacian. We then obtain the wave equation:

$$(\nabla^2 - \frac{1}{c^2}\frac{\partial^2}{\partial t^2})\mathbf{E} = \frac{1}{\epsilon_0 c^2}\frac{\partial^2 \mathbf{P}}{\partial t^2} \tag{2.4}$$

This equation is the theoretical foundation of the work presented here. Linking time and spatial evolution, it governs the electric field's propagation. The response of matter is captured by the non-zero polarization field, appearing as the source-term of the wave equation. In the case where no material is present, the right hand side becomes null: it falls back to the study of propagation of a plane wave through vacuum. In the presence of a material, its response is entirely represented by the polarization field $\mathbf{P}$. This field is the electric field produced by the electric dipoles (nuclei and their surrounding electronic clouds) constitutive of matter. The quest for manipulation of the light-matter interaction to our benefit is reduced to the study of the polarization term. Being proportional to the displacement, the second time derivative of the polarization term directly indicates the possibility of accelerating charges to contribute a radiation field to the total electric component of the field described in the wave equation. Understanding of this source term, especially under strong illumination, is the starting point of this work and will motivate the manipulations done later.

2.1 Terahertz generation and detection in nonlinear media

2.1.1 Optical rectification and electro-optic sampling in $\chi^{(2)}$ media

In the presence of an external field, matter produces a polarization field as a response. The nature and strength of the external field, together with the details of the material's response determines the polarization field. With respect to the strength of the incoming field, two types of responses are expected. A linear response when the field is not strong enough to change the material illuminated. A non linear response when the field is strong enough to affect the state of the material. In this case, we can again distinguish two broad scenarios: perturbative and non perturbative. Perturbative response arises when the applied field is smaller than a characteristic field associated with the binding mechanism participating in the polarization response. On the contrary, non-perturbative regime arises when applied field is equal to or exceeds such limit, resulting, for example, in processes such as tunnel ionization and high-harmonic generation. In this text, we will be focusing on the perturbative regime, where the response can be properly approximated by a Taylor expansion. The polarization

field is then given by :

$$\mathbf{P}(\mathbf{E}) = \epsilon_0 \left[\chi^{(1)} \vdots \mathbf{E} + \chi^{(2)} \vdots \mathbf{E} \cdot \mathbf{E} + \chi^{(3)} \vdots \mathbf{E} \cdot \mathbf{E} \cdot \mathbf{E} + \dots \right] = \mathbf{P_L}(\mathbf{E}) + \mathbf{P_{NL}}(\mathbf{E}) \tag{2.5}$$

where $\mathbf{E}$ is the external electric field, ϵ_0 is the vacuum permittivity, $\chi^{(n)}$ is the susceptibility tensor of rank n associated with the material and $\vdots$ represents the tensorial product. The first term of the expansion, linear in $\mathbf{E}$, represents the linear part of the response, $\mathbf{P_L}$. The non linear response, $\mathbf{P_{NL}}$, is then represented by the other terms. By the nature of the linear term, it will always produce a polarization at the same frequency as the input field. As such, it can not be used for generating new frequencies, which is possible for higher terms, as we see below. Inserting this expansion of the polarization into the wave equation 2.4 and moving $\mathbf{P_L}$ to the left, we obtain the non-linear wave equation:

$$(\nabla^2 - \frac{(1+\chi^{(1)})}{c^2}\frac{\partial^2}{\partial t^2})\mathbf{E} = (\nabla^2 - \frac{\mathrm{n}^2}{c^2}\frac{\partial^2}{\partial t^2})\mathbf{E} = \frac{1}{\epsilon_0 c^2}\frac{\partial^2 \mathbf{P_{NL}}}{\partial t^2} \tag{2.6}$$

where n is the frequency dependant and complex valued refractive index of the material and we define $\epsilon \equiv \epsilon_0(1+\chi)$, its permittivity. In linear optics, the refractive index governs reflection and refraction at an interface between two materials on one hand, and propagation speed through a material on the other. The speed at a given frequency, called phase velocity, is $v_p = c/\mathrm{n}(\omega)$. The envelope of a wave packet, composed of waves at different frequencies, travels in the medium at the group velocity v_g [11]:

$$v_g = \frac{c}{\mathrm{n}(\omega) + \omega\frac{\partial \mathrm{n}(\omega)}{\partial \omega}} \tag{2.7}$$

The difference between phase and group velocity means that travel through a medium changes the temporal shape of the wave packet according to its refractive index, a phenomenon called dispersion.

For the rest of this subsection, the focus will be on the first term of $\mathbf{P_{NL}}$ in equation 2.6. This term is associated with non-linear effects of second order, also called $\chi^{(2)}$ effects. By specifying the external input field, we can predict the spectral content of the response of a $\chi^{(2)}$ material under strong irradiation. To illustrate the action of this term, we represent our incoming field along any one direction as a discrete sum of plane waves :

$$\begin{cases} E_{in}(t) = \sum_{j=1}^{n}[E_j \exp(i\omega_j t) + c.c] \\ E_j \equiv E_j(\omega) = A_j \exp(-i\mathbf{k}_j \cdot \mathbf{r}) \end{cases} \tag{2.8}$$
$$\Rightarrow E_{in}(\omega) = E_1 \exp(i\omega_1 t) + E_2 \exp(i\omega_2 t) + c.c$$

where $c.c$ is the complex conjugate, ω is the frequency, t the time, $\mathbf{r}$ the position vector, $n = 2$ is the order of the non linear effect under consideration, and $\mathbf{k}$ is the wavevector with a magnitude $k = \mathrm{n}\omega/c$. As such, the spectral content of the non linear polarization field follows :

$$\begin{aligned} P_{NL} \propto E_{in}^2 = [\ E_1^2 \exp(i2\omega_1 t) + E_2^2 \exp(i2\omega_2 t) + c.c\ ] + [\ 2|E_1|^2 + 2|E_2|^2\ ] + \\ [\ 2E_1E_2 \exp(i(\omega_1+\omega_2)t) + c.c\ ] + [\ 2E_1E_2^* \exp(i(\omega_1-\omega_2)t) + c.c\ ] \end{aligned} \tag{2.9}$$

where squaring of the input field is motivated by equation 2.5. The polarization field terms have been separated into four groups with similar characteristics. The first group shows the appearance of a spectral response at frequencies doubling ω_1 and ω_2, a phenomenon called second harmonic generation (SHG). The second group, associated with the process called optical rectification (SHG), shows nonlinear mixing that produces a quasi-stationary (i.e. a direct current, DC) field, akin to a voltage across the sample. Sum frequency generation (SFG) and difference frequency generation (DFG) are respectively identified to the third and fourth group. As the name indicates, they are associated with spectral responses at frequencies corresponding to a sum or a difference, respectively, of the frequencies considered in the exciting field. The total field produced by the non linear processes at a given frequency is obtained by integration over all possible ω_1 and ω_2 within the spectral content of the source. As indicated in the introduction of this chapter, the polarization field is the field

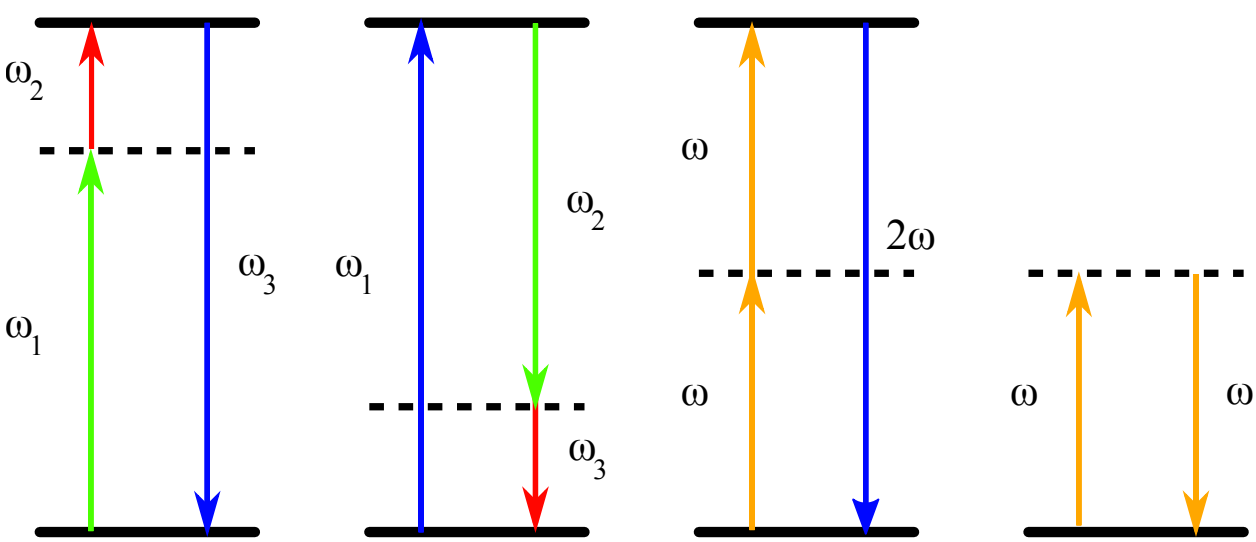

Figure 2.1 $\chi^{(2)}$ phenomena energy-level diagrams. **From left to right :** Sum-frequency generation, difference frequency generation, second harmonic generation, optical rectification.

produced by electric dipoles in the material. More specifically, it is the field produced by their oscillation around their equilibrium positions. The particular configuration of the considered

material gives it specific frequencies at which it vibrates, called resonant frequencies. In quantum mechanics, these frequencies correspond to energy levels at which interaction with the field is strong and relatively stable. When the frequency considered is not resonant, the state reached is unstable and vanishes quickly. These non-observed states are useful for a phenomenological understanding of the interaction and are rightfully labeled virtual states. For the $\chi^{(2)}$ processes listed here, the energy level diagrams representing them are shown in figure 2.1, with the virtual states shown with dashed lines. The exciting field in each scenario is represented by an upward arrow, with the contrary for an emitted field.

Going back to equation 2.9, we consider the case where the input frequencies are similar, $\omega_1 - \omega_2 = \delta\omega \equiv \Omega$. The electrical field is:

$$E^2 = [(E_1^2 + E_2^2)\exp(i2\omega t)] + [2|E_1|^2 + 2|E_2|^2] + [2E_1E_2\exp(i2\omega t)] + [2E_1E_2^*\exp(i\Omega t)] \quad (2.10)$$

where the addition has been rounded to 2ω. In this case, DFG becomes similar to OR, as the generated field is close to steady. Also called OR, this process produces terahertz radiation for an exciting field in the near infrared. By appropriate choice of the detection method, the higher frequency components are discarded and the polarization generated is reduced to:

$$P_{NL} \propto E_1E_2^*\exp(i\Omega t) \quad (2.11)$$

where the proportionality constant is given by the frequency dependent $\chi^{(2)}$ tensor. Sufficiently away from the response poles of this tensor, the total bandwidth (frequency extent) of the THz emission process is then determined by the Fourier transform of the intensity envelope of the generating pulse and its shape is modulated by the non-linear tensor [12].

The same mixing product can also be used for THz detection. To showcase this, we set ω_2 to a near DC value in eq. 2.9 to obtain:

$$E^2 = [\ 2|E_1|^2 + 4|E_2|^2\ ] + [\ E_1^2\exp(i2\omega_1 t) + 4E_2E_1\exp(i(\omega_1)t) + c.c\ ] \quad (2.12)$$

where we still have a DC field, a field at $2\omega_1$ and a field at ω_1. By spectral filtering, we can eliminate the contribution of the first 2. We then have :

$$P_{NL} \propto E_2E_1\exp(i(\omega_1)t) \quad (2.13)$$

where it is clear that the non linear response is, in fact, linear with respect to the input field $\mathbf{E}_1$. The scenario of the linear response effectively implies a change to the refractive index of the probe field ($\mathbf{E}_1$), induced by the application of the quasi-stationary field ($\mathbf{E}_2$). Utilization

of this refractive index change for THz detection is called electro-optic sampling (EOS), where the frequency of the quasi-DC field is assumed small compared to the bandwidth of the probe [13]. A more rigorous treatment is done by replacing the near DC term by a THz frequency component at Ω. The previous equation is then replaced by:

$$P_{NL} \propto E_2 E_1 \exp(i(\omega_1 + \Omega)t) + E_2^* E_1 \exp(i(\omega_1 - \Omega)t) \tag{2.14}$$

The EO effect is then a combination of DFG and SFG. The spectrum of the produced nonlinear polarization field might overlap with the input field. When they do, they interfere and the EO effect is reduced to a change in refractive index in the medium as in the near-DC case which can be used for field-resolved detection. The general case provides insights into the functioning of DFG and SFG. The field at $\omega_1 \pm \Omega$ corresponds to a shift to the right/left of the probe field at ω_1. As such, the greater Ω is, the less overlap there is and spectral filtering becomes a tool of discrimination against one of these effects, also useful to reduce the detection noise potentially arising from the frequency components of the probe that are outside the spectral overlap region. For small Ω, the SFG and DFG fields mostly overlap with one another, along with the probe. The latter motivates the interpretation that the EO effect is just a change in refractive index for near-DC fields. In EOS, the EO effect used together with an adjustable delay between the THz and the probe fields, one can measure the total evolution of the THz field and hence, upon Fourier analysis, the complex-valued frequency components of the THz field [14]. The highest frequency detectable with EOS arises from the limitation of the bandwidth of the probe [15].

Once the non-linear polarization of interest is established, we can insert it in equation 2.4 to get a coupled wave equation linking the input field with the produced field. In this text, the non-linear effects considered are small perturbations. As such, the plane wave approximation for the field is maintained for the produced field. Perturbative treatment also means that the pumping field is considered weakly depleted. We also consider the carrier frequencies to oscillate much faster than the envelope changes, also called the slowly varying approximation. With these assumptions, we find the THz field produced to be [15] :

$$E_{THz}(\Omega, t) = i \int_0^\infty \frac{2\pi\omega^2}{c^2 k(\Omega)} \chi^{(2)}(\omega; \omega - \Omega; \Omega) \zeta_- E_1(\omega) E_2^*(\omega + \Omega) \exp(-i\Omega t) d\omega \tag{2.15}$$

with ζ_- the phase matching factor, discussed later. The fields for SFG and DFG are of a similar form.

With the theory to link input fields to the produced fields established, we also have to look at the best way to find suitable materials. An important criterion for the choice of the

material is given by a classical understanding of the $\chi^{(2)}$ response at the microscopic level. Complementary to the purely mathematical way of obtaining the polarization used here, we now introduce a model of light-matter interaction that enables us to model polarization field associated with the displacement of electrons in a weakly anharmonic approximation of the shape of the binding potential, in other words a Lorentz model of an anharmonic response. This Lorentz model establishes the link between the polarization field and the excitation field through physical considerations. The Lorentz oscillator model for the optical response of bound charges can be updated to a non-linear version. In order to do so, the potential yielding the conservative force in the linear model is updated to include higher order terms of the Taylor expansion. Introduction of a next-order response establishes a cubic dependence of the confinement potential on the position, in turn leading to $\chi^{(2)}$ optical response [10]. The cubic term doesn't obey the centrosymmetry of the potential : only a non centrosymmetric medium can have a second order non linear response to an external excitation.

The permittivity, as well as the refractive index to which it is linked, are the practical quantities through which the response of a material to radiation is evaluated. The Lorentz oscillator model gives us the frequency dependant contribution to the permittivity from the electrons in the material. On the other hand, a harmonic oscillator model for the interatomic interaction gives us the frequency dependant contribution from the crystal to the permittivity [16]. In the case of crystalline media with multiple atoms, there is a splitting in the band diagram giving us quantized collective vibration of the crystal (phonons) at different frequencies. For diatomic heteronuclear molecules, such as group III-V and II-VI semiconductors, for example, the lowest splitting in the band diagrams separates tranverse optical (TO) and longitudinal optical (LO) phonon. In this region, the refractive index is purely imaginary with a high magnitude: the material is highly absorptive. Also, this spectral region has a real negative permittivity. It means that the created polarization opposes the creating excitation: there is reflection. Vibration theory of crystals and the Lorentz oscillator model thus tell us that between the TO and LO, there is a zone of strong reflection where any penetrating radiation is absorbed: this is the Reststrahlen band, where the semiconductor materials cannot generate or transmit radiation, for sufficient thickness of the material.

2.1.2 Phase matching

While the $\chi^{(2)}$ phenomena occur concurrently, they remain different with regards to respective efficiency. The plane waves produced at each frequency must respect the form described in

eq.2.8, raising additional conditions for observing SFG and DFG:

$$\begin{aligned} \omega_{3,4} &= \omega_1 \pm \omega_2 \\ \mathbf{k}_{3,4} &= \mathbf{k}_1 \pm \mathbf{k}_2 \end{aligned} \tag{2.16}$$

with indices $3, 4$ associated with SFG and DFG respectively. The first equation represents the conservation of energy in the interaction. The second one, called the phase matching condition, represents the conservation of momentum and limits the efficiency of those phenomena. For our purposes, we consider only the case in which $\mathbf{k}_1$ and $\mathbf{k}_2$ are collinear. The phase matching condition then reduces to :

$$\mathrm{n}_{3,4}\omega_{3,4} = \mathrm{n}_1\omega_1 \pm \mathrm{n}_2\omega_2 \tag{2.17}$$

where n_i is the refractive index. In practice, the quality of the phase-matching is evaluated by the phase mismatch:

$$\Delta k_{\pm}(\omega, \Omega) = -k(\omega) \pm k(\Omega) + k(\omega \mp \Omega) \tag{2.18}$$

This mismatch affects the efficiency of SFG and DFG through the phase matching factor:

$$\zeta_{\pm} = \frac{\exp[i(\Delta k_{\pm}(\omega, \Omega)l)] - 1}{i(\Delta k_{\pm}(\omega, \Omega))} \tag{2.19}$$

where l is the length of the crystal. Since the intensity of the field scales as its square, we can appreciate the effect of phase matching on the intensity. By squaring the real part of $\zeta_{\pm}$, we obtain:

$$|\zeta_{\pm}| = l^2 \mathrm{sinc}^2(\Delta k l/2) \equiv l^2 \mathrm{sinc}^2(l/(2l_{coh})) \tag{2.20}$$

where $l_{coh} = 1/\Delta k$ is the coherence length of the phase mixing in the material. This equation highlights the physical processes behind phase matching [10]. l is the interaction length over which the SFG/DFG occurs. As such, the longer the distance, the more contributing photons are produced. The sinc term on the other hand represents the relative phase of these contributing photons when there is no phase-matching. For a propagation distance lower than the coherence length, the driving polarizations are relatively in phase with the induced polarization. As such, power flows from the driving polarizations towards the SFG polarizations. Beyond the coherence length, the accumulated relative phase is too high and the power flows back from the induced polarization to the driving ones: efficiency drops. The contribution from the interaction length balances the loss of efficiency caused by non-phase matching, as seen in figure 2.2 which compares the efficiency for the SFG effect between

the phase matched and non phase matched cases. The phase-matched case has all the contributing photons in phase: the intensity rises quadratically with the propagation length.

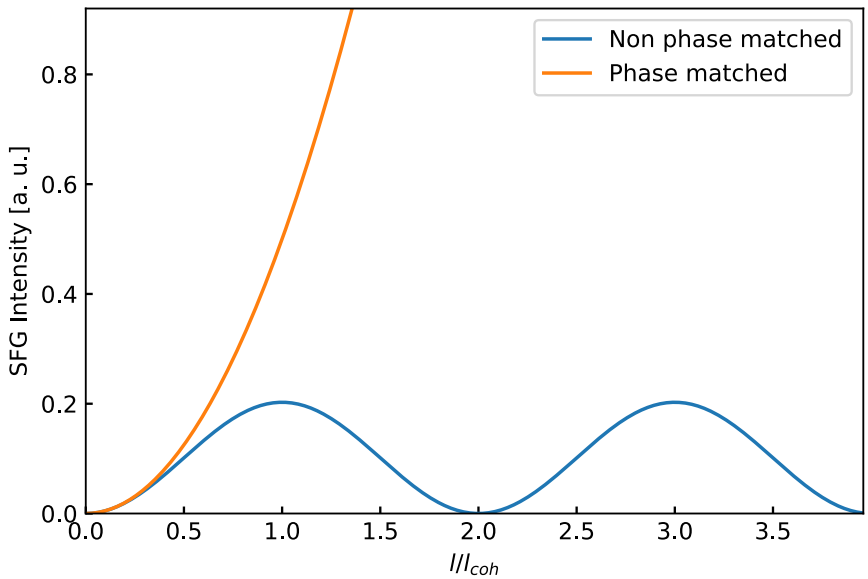

Figure 2.2 Efficiency of SFG in phase-matched and non-phase matched configurations.

Since no real material is dispersionless, the phase matching condition is satisfied by exploiting other properties of materials and their refractive indexes. The most popular of these techniques is birefringent phase matching in uniaxial crystals [11]. The ordinary and extraordinary polarizations in an uniaxial birefringent crystal have different refractive indexes. Phase matching is then achieved by choosing the angle of incidence, with respect to the orientation of the optical axis, of the input field in such a way that the condition is satisfied for one polarization at the output. This creates two categories for phase matching in uniaxial birefringent crystals, simply named type I and type II phase-matching. In type I, the two input polarization are the same, which is orthogonal to the produced polarization. In type II, the input polarizations are orthogonal to one another. Type II phase matched optical rectification is the initial method for broadband THz generation that this text looks to improve on, while type II phase matched EOS is the technique for broadband THz detection used in this text.

2.1.3 Distortion in an EOS set-up

The theory presented in this section paints a good qualitative image of OR and EOS. However, a practical description of OR and EOS has to account for the impact of an usual EOS set-up on the THz waveform [17]. In such a set up, as we will see in more detail in section 4.1, the generated THz electrical field E_{THz} will exit the generation crystal and propagate towards the EO crystal where it is detected, going through collection and focusing optics (off axis-parabolic mirrors), filtering optics for the pump beam. Most of the effects occurring over this propagation distance are within the scope of linear optics, and affect the THz radiation through a linear transfer function which is the product of functions associated to each effect. We go over the most important effects to consider and their associated functions here.

After the THz field is produced inside the OR crystal, it leaves the crystal through a crystal/air interface. At this interface, a reflection can also occur from the front and then the back interfaces. If the distance between the two is small compared to the wavelength of THz radiation, the Fabry-Perot effect occurs. Fresnel coefficients dictate how transmissions and reflections occur, inward or outwards through:

$$\begin{cases} \begin{cases} R_{in}(\omega) = (\sqrt{\epsilon} - 1)/(\sqrt{\epsilon} + 1) \\ T_{in}(\omega) = 2/(\sqrt{\epsilon} + 1) \end{cases} & \text{at the air-crystal interface} \\ \begin{cases} R_{out}(\omega) = (1 - \sqrt{\epsilon})/(\sqrt{\epsilon} + 1) \\ T_{out}(\omega) = 2\sqrt{\epsilon}/(\sqrt{\epsilon} + 1) \end{cases} & \text{at the crystal-air interface} \end{cases} \tag{2.21}$$

for normal incidence. Then, the FP transfer function is:

$$T_{FP}(L, \omega) = \frac{1}{1 + R_{out}^2 \exp(i2n_{THz}\omega L/c)} \tag{2.22}$$

with L the length of the crystal, c the speed of light in vacuum and n_{THz} the refractive index of the emitted field in the crystal.

At the OR crystal, the input field is focused to reach high enough intensities for OR. Then, E_{THz} has a small point source and diffracts until the point where it is collected. Due to the broadband content of the generated THz radiation, different wavelengths diffract with different angles, suffering diffraction losses at the optical elements of finite size. For conditions with strong focusing and broadband source character, the paraxial approximation does not always hold and Behte's diffraction theory comes into play. We then have two regimes with

different transfer functions.

$$T_{diff}(\omega) = \begin{cases} \left(1 - \exp(-\frac{\tan^2(\theta_{coll} k^2 r_0^2)}{4})\right)^{1/2} & \text{for } kr_0 > 1(\text{paraxial}) \\ \frac{2\sqrt{2}k^2 r_0^2}{3\pi}\left(\frac{8}{3} - \frac{5\cos(\theta_{coll})}{2} - \frac{\cos(3\theta_{coll})}{6}\right)^{1/2} & \text{for } kr_0 < 1(\text{Bethe}) \end{cases} \tag{2.23}$$

where $\theta_{coll} = \arctan(1/2f_{\#})$ and $f_{\#}$ is the f-number of the collection optics.

After the collection, the THz field goes through a filter for the pump. In the special use case where spectroscopy is done, it also goes through the sample. The filter, much like a sample, has two interfaces where reflections and transmissions occur following the respective Fresnel coefficients. We obtain the transfer function trough the filter (or a sample):

$$T_{filter}(L, \omega) = \frac{T_{in}T_{out}}{1 + R_{out}^2 \exp(i2n_{THz}\omega L/c)} \exp(in_{THz}\omega L/c) \tag{2.24}$$

The THz is detected at the EOS crystal. The THz field has to be focused in order to contribute to the EO effect. The transfer function is simply the ratio of the size of the beam at the focusing optics $r_{in}(\omega)$ with its size on the detection crystal $r_{foc}(\omega)$:

$$T_{focus}(\omega) = \frac{r_{in}(\omega)}{r_{out}(\omega)} \tag{2.25}$$

The field at the EO crystal is then:

$$E_{det} = T_{out}T_{FP}T_{filter}T_{diff}T_{focus}E_{THz} \equiv f(\omega)E_{THz} \tag{2.26}$$

where $f(\omega)$ is the frequency dependant transfer function of the THz throughout the EOS set-up.

2.2 Spintronic emission of terahertz radiation

A novel way to generate terahertz radiation is found in spintronic emitters. As hinted by the name, spintronic emitters exploit the added degree of freedom granted by spin to open new opportunities for electronics. In this particular case, it is done by use of a heterostructure with (at least) two metallic nanometer-thick layers, one ferromagnetic and the other non ferromagnetic, and the structure is subjected to an externally applied magnetic field, controlling the polarization state of the emitted THz radiation. The demonstration of spintronic devices is still rather recent and much research continues to be devoted to understanding the microscopic nature of the THz generation in such devices. This section summarizes

presently-accepted phenomenological understanding of such process, and what it entails for the immediate future of terahertz generation.

In their simplest form, THz emission from spintronic devices relies on an interplay of time-sequence of three mechanisms, as shown in figure 2.3 [18]. First, there is an ultrafast heating of the electrons in the ferromagnetic layer, immersed in an external magnetic field. Conditions in the FM layer are favorable to supporting a spin current j_s, launched into the bulk of the material in a direction perpendicular to the sample surface. Afterwards, the forward propagating current is polarised with regards to spin, in that same layer. Finally, the electrons in that spin polarised current are scattered in the directions normal to that of the spin current, labeled j_c in figure 2.3. Thus, transverse character of time-varying charge current in the NM layer acts as a source of dipole emission, in the original direction of the excitation and at frequencies, approximately contained in the temporal envelope of the exciting pulse.

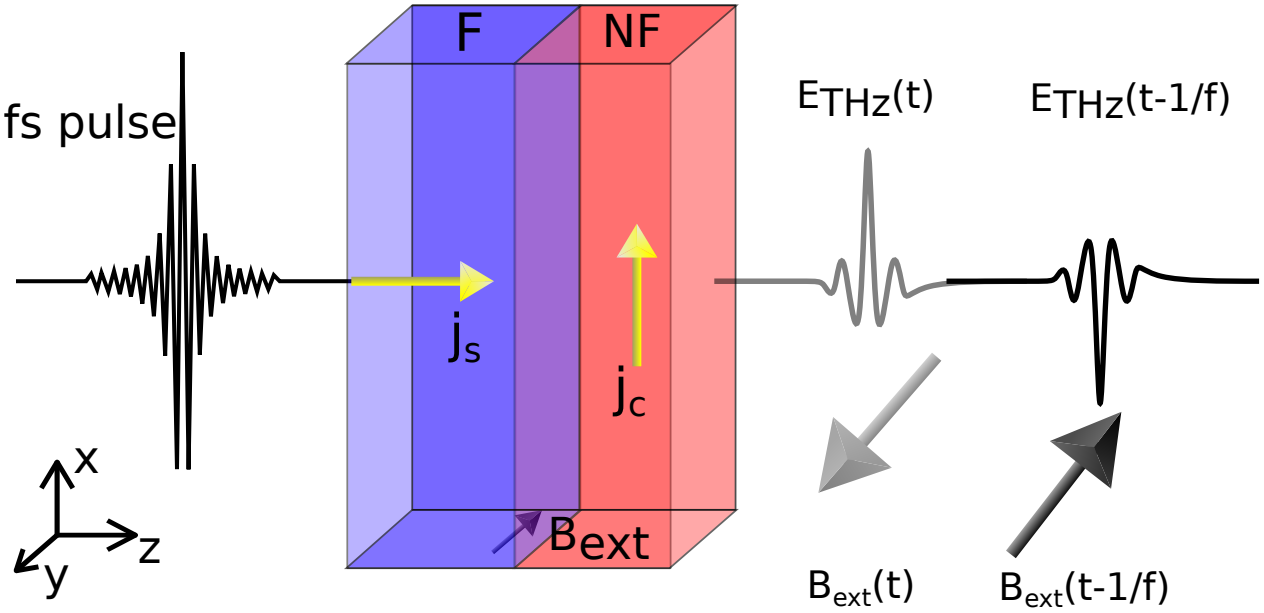

Figure 2.3 Schematic of the spintronic emitter. F: ferromagnetic layer, NF: non ferromagnetic layer, j_s: spin current, j_c: electrical current.

Ultrafast heating of the ferromagnetic layer is done by an ultrafast optical pump. This causes a change in the distribution of majority and minority spin electrons in the layer, under applied external B-field bias. As such, the heating lessens the magnetization setup by the external field, by loss of the large scale ordering of the spins. This phenomenon, called ultrafast demagnetisation (UDM), is understood through the three temperature model [19] [20]. The three temperatures under consideration are T_e, T_s and T_l, respectively associated with the electrons, the spins and the lattice vibrations (phonons). A Fermi-Dirac distribution of the

electron energies is characterized by the temperature T_e. Defined as the temperature yielding the observed distribution of spins, T_s is a not a "real" temperature by the usual definition. T_l is the temperature associated with total amount of phonon energy. A representative calculation of the dynamics in a 3-step model is shown in figure 2.4 In the three temperature model,

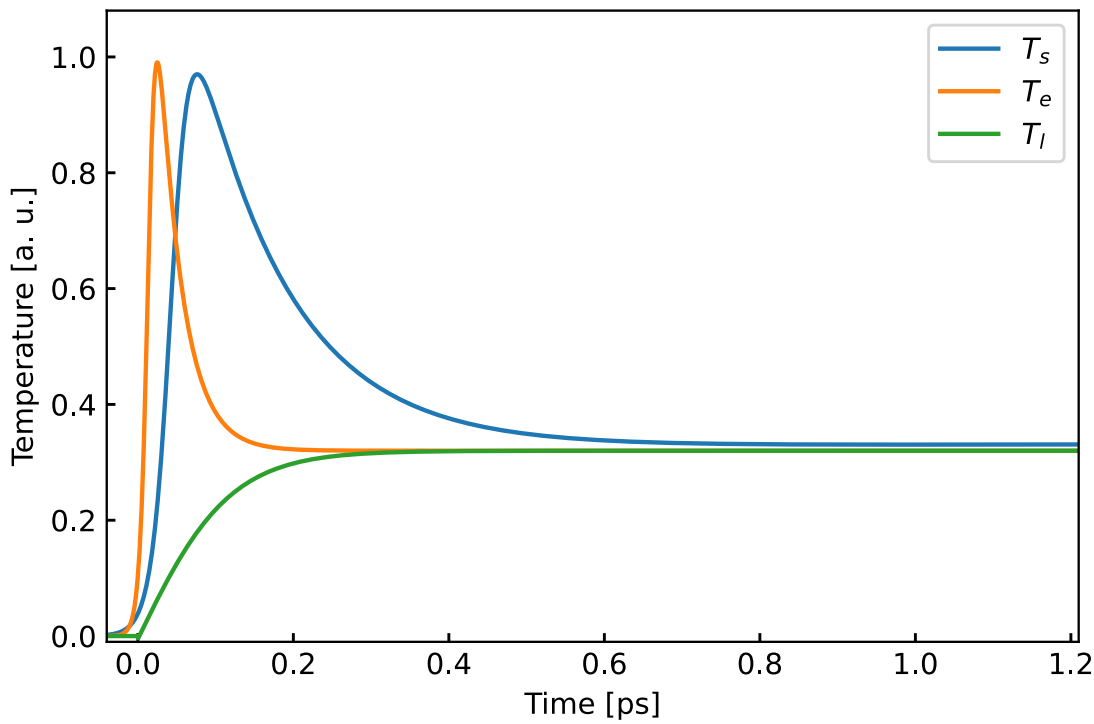

Figure 2.4 Schematic of the three temperature model. T_e: electron temperature, T_s: spin temperature, T_l: phonon temperature.

these three "baths" are coupled one to another. First, the electrons are moved to an out of equilibrium distribution of energy by the ultrafast optical pulse, as seen in figure 2.5(a). This opto-electronic process has no effect on the spin distribution as optical excitations in metals are spin conserving (transitions under dipole approximation). A quasi-thermal distribution within the electronic system is first regained through the energy exchange mediated by the electron-electron interaction. On timescales below 100 femtoseconds (fs), the thermalization is dominated by the electron-electron scattering rates. On longer timescales, inelastic collisions of hot electrons with phonons results in loss of energy (cooling) of the electronic bath by transferring of its energy to the phonon subsystem, rising T_l on a characteristic timescale of several picoseconds(ps). Electron-phonon scattering can sometimes be accompanied by flipping of the spin state of the electron (figure 2.5(b)). This spin-flipping event changes the

distribution of spin state in the material, meaning a change in the spin temperature. While the processes underlaying ultrafast demagnetization are still investigated, spin-flips are currently the main candidate for the driving force in UDM [21]. Spin-flip probability is correctly described by the Elliott-Yafet scattering model in this circumstance and is proportional to $n^{F\uparrow}(\epsilon, t) - n^{F\downarrow}(\epsilon, t)$, the difference in occupation number of Bloch states of energy ϵ, with majority(↑) or minority(↓) spins in the F layer at a given moment t [22]. In the Fermi-Dirac distribution considered, each occupation number $n^{F\sigma}$ has an associated chemical potential $\mu^{F\sigma}$ with σ the spin state.

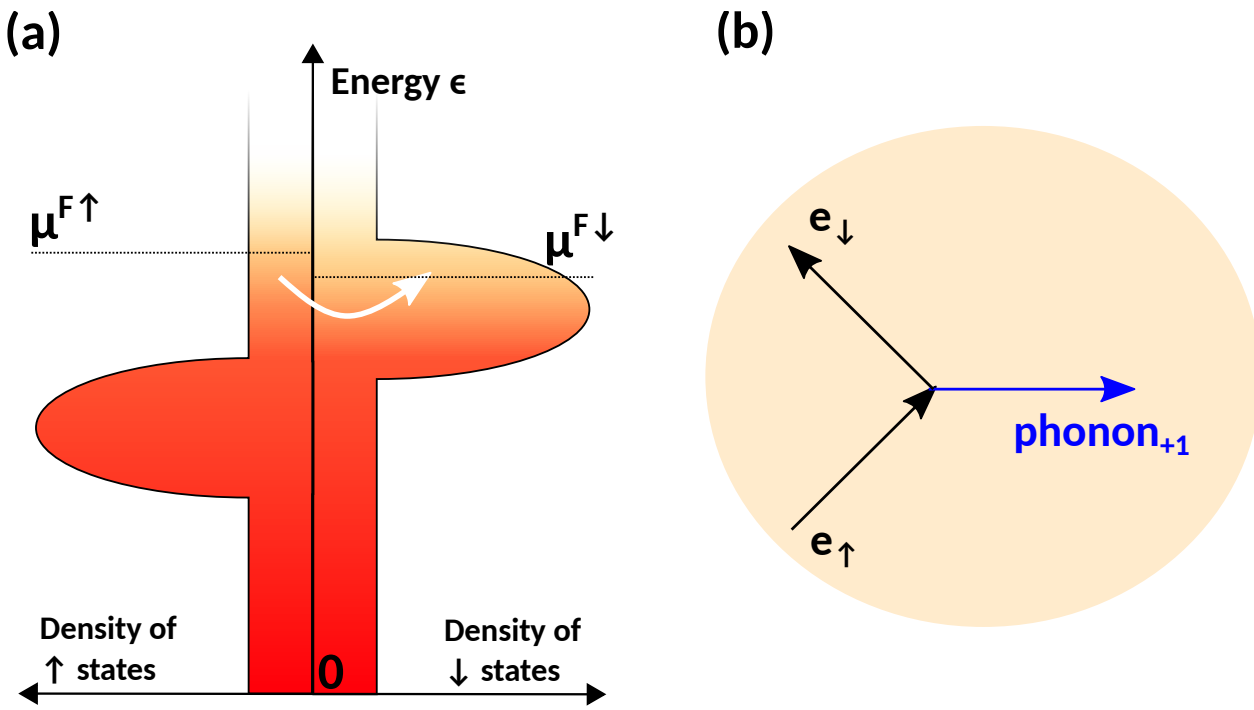

Figure 2.5 (a) Schematic of the band diagram in the F layer. The Fermi level for each spin state is shown, with passage from one to the other mediated by spin flips (white arrow). (b) Schematic of the electron-phonon scattering inducing the spin flip.

Boltzmann's equation of transport dictates the flow of electrons in the heterostructure: they flow from the zone with a high density of excited electrons (interface heated by pump), towards the bulk, a phenomenon called ultrafast spin transport [23]. The nanometer thickness of the ferromagnetic layer ensures that this movement occurs in the ballistic regime. The electrons in this forward current will have their spins realigned according to the local magnetization, through exchange interactions. The electronic current becomes spin polarised. Because the electronic current is generated as soon as the layer is heated, the material has yet to reach the homogeneity of spin distributions mentioned above, which is why $\mathbf{j}_s$, the current at the interface between the two layers, is strongly spin polarised and accounts for

all spin transmission events across the interface. In this case also, the driving mechanism behind the current is the difference in occupation of the spin states [21]:

$$j_s(t) \propto \Delta\mu_s(t) = \int d\epsilon \left(n^{F\uparrow}(\epsilon, t) - n^{F\downarrow}(\epsilon, t) \right) \tag{2.27}$$

where $\Delta\mu_s$ can be linked to the spin voltage $\mu^{F\uparrow} - \mu^{F\downarrow}$. As such, $\Delta\mu_s$ can be considered a generalized spin voltage.

In the non ferromagnetic layer, the incoming spin current is transformed into an electrical current, $\mathbf{j}_c$, by the inverse spin hall effect. This phenomenon transforms a spin current into an electrical one through the spin orbit coupling, deviating different spins in opposing directions. The two currents are linked by [23] :

$$\mathbf{j}_c = \frac{2e}{\hbar}\theta_{ISHE}\mathbf{j}_s \times \boldsymbol{\sigma} \tag{2.28}$$

where $\boldsymbol{\sigma}$ is the direction of the spin polarization, θ_{ISHE} is the angle of the deviation. The angle then quantifies the strength of the effect, which is naturally stronger for heavy metals with strong spin-orbit interaction. The orthogonal acceleration of electrons is the source of the terahertz radiation and completes the presentation of the phenomena responsible for spintronic emission. The strength of the emitted terahertz field is given by [18] :

$$E(\omega) = \frac{2Z(\omega)e^2}{\hbar} \int_0^d \theta_{ISHE}(z, \omega) j_s(z, \omega) dz \tag{2.29}$$

where $Z(\omega)$ represents an impedance associated with the effectiveness of the process, d is the thickness of the layer. This generalized Ohm's law can be integrated over the thickness of the emitter, leaving an electric field that is dependant on the frequency varying impedance, spin Hall angle and spin current. Over the frequency ranges of interest, current measurements show that the first two are frequency independent. As such, over the range of interest, we have:

$$E(t) \propto j_s(t) \propto \Delta\mu_s(t) \tag{2.30}$$

in the time domain. The linear dependence of the emitted field on the generalized spin voltage offers the opportunity to study the timescales of the underlying relaxation processes in the spintronic emitter. Generalized spin has been entirely described using the electron-spin (Γ_{es}^{-1}) and electron phonon (Γ_{ep}^{-1}) relaxation times along with the ratio of electronic to total heat capacity of the emitter R [21]:

$$E(t) \propto \Delta\mu_s(t) \propto \Theta(t) \left[A_{es} \exp(-\Gamma_{es} t) - A_{ep} \exp(-\Gamma_{ep} t) \right] \tag{2.31}$$

where $A_{es} = (\Gamma_{es} - R\Gamma_{ep})/(\Gamma_{es} - \Gamma_{ep})$ and $A_{ep} = (1 - R)\Gamma_{ep})/(\Gamma_{es} - \Gamma_{ep})$ and $\Theta(t)$ is the Heaviside step function.

The phenomena described above are associated with other effects to enhance the performance of spintronic emitters. One such effect is the Fabry-Perot effect. The small thickness of the layer ensure that it is, for most optical pumps, much smaller than the wavelength of the pump. As such, reflection echoes of the pump and the radiated THz interfere constructively at the interfaces. When taking into consideration the expected strengthening of the radiated field for higher thickness suggested by equation 2.29, there is a thickness for which the emission is maximized. Reflections at the interface have another consequence: the generation of a spin polarized current is also done when the pump is reflected at the interface between ferromagnetic and non ferromagnetic layers. This opposite spin polarized current can be exploited by having another non ferromagnetic layer before the ferromagnetic layer. By choosing it to have similar in magnitude but opposite in value spin-orbit coupling to the other non ferromagnetic layer, the reflection of this back emitted THz radiation and the forward emitted THz radiation interfere constructively : a tri-layer spintronic emitter emits stronger terahertz radiation.

It was mentioned earlier that the initial current in the ferromagnetic layer is spin polarized by local electron interaction and that the spin current dictates the orientation of the current generating the THz. Those dependencies cause the polarization of the THz radiation to be directly connected to the local magnetization in the ferromagnetic layer, to which it is orthogonal. When immersed in an external magnetic field, the magnetization of a ferromagnet depends on the orientation of the field. The orthogonality between the orientation of the external magnetic field in which the emitter is immersed and the radiated field means that modulation of the THz field is possible by modulation of the external magnetic field. It is important to note that it was demonstrated that the emitted field scales linearly with the external B field, until it reaches an saturation value. The emitted field also scales linearly with the incident pump power, while the wavelength of the pump is irrelevant to the observed effect. This confirms the idea that T_s changes by interaction of 'secondary' excited electrons.

Overall, the spintronic emitters have been demonstrated as broadband gap-less terahertz emitters that do not require phase matching, because of the thinness of the layers involved. They have been optimized to emit THz fields comparable in strength to those obtained from optical rectification. The possibility of high frequency modulation through the external B field is makes it an excellent candidate for high sensitivity measurement, limited only by the optical noise from the source. The THz field emitted also offers insights into the functioning of the heterostructure, which could lead to improvements in the future, while deepening our

understanding of ultrafast electronic interactions in metals.

2.3 Relative intensity noise

Modern instruments have substituted optoelectronics systems to the eye as a mean of image formation. The electrical response they produce by converting the photons under study make a photocurrent. Whether it is analog or digital, this photocurrent contains the contribution from converting the photons of interest, called signal, as well as contributions from other sources, called noise. Noise as an unwanted contribution can be divided in two categories [24]: the background, product of the conversion of a consistent optical contribution in the system under study and the random noise, raising from random photonic fluctuations or from the process of converting, amplifying or quantizing the input.

Adequate understanding of noise, its sources and how it transfers through the set up is crucial to achieve high sensitivity measurements. In this thesis, the generation and detection of THz radiation are reliant on the laser, it is then clear that a fundamental understanding of its functioning is also required to characterise the noise.

The steady state operation of a passive mode-locked laser, such as the one used in this thesis, is understood through the Haus master equation [25]. In this theoretical frame, noise from a Kerr lens mode-locked(KLM) laser is handled by soliton perturbation theory. It finds its source in gain fluctuations, cavity length fluctuations and spontaneous emission fluctuations. These fluctuations give rise to the phase fluctuations, the pulse-to-pulse phase slip, the timing jitter and the amplitude fluctuations, respectively represented by $\Delta\theta(t)$, Φ_{CE}, $\Delta T_R(t)$, $\Delta A_0(t)$ in :

$$A(t) = [A_0 + \Delta A_0(t)] \sum_{m=-\infty}^{+\infty} a(\ t - mT_R + \Delta T_R(t)\ )\ \exp[\ i(\ \omega_0 t + m\Phi_{CE} + \Delta\theta(t)\ )\ ] \quad (2.32)$$

where A_0, ω_0, T_R are respectively the peak amplitude, the central frequency and the cavity round trip time. $a(t)$ is the solitonic solution to the master equation of a steady-state operating KLM laser:

$$a(t,T) = A_0 \operatorname{sech}\left[\frac{1}{\tau}(t - t_0)\right]^{(1+i\beta)} \exp\left[i\left(\phi\frac{T}{T_R} + \theta\right)\right] \quad (2.33)$$

where θ is the phase of the pulse, β is the chirp parameter, t is a short-term time variable (shorter than a cavity round trip), T is a long-term time variable (many cavity round-trips), t_0 is proportional to T and ϕ is the phase shift produced per pass. A more rigorous treatment of the Haus master equation and the solitonic solution is beyond the needs of this text and

is not included.

This thesis considers THz emission from spintronic devices. Given current understanding of the emission process (see section 2.2), the process is not sensitive to the shape of the carrier wave under the envelope, hence the only fluctuations that would be of primary relevance are those of the amplitude. As seen in equation (2.32), it implies disregarding the impact of the phase fluctuations as well as the pulse-to-pulse phase slip. The amplitude noise can be analyzed through relative intensity noise (RIN) characterization. It quantifies the deviation from the average laser power at a given frequency. The mathematical formalism around RIN characterization is developed under three assumptions [26]. The Markovian assumption that correlation time of the noise sources is much shorter than the relaxation times of the system is the first one. The second one is that the noise sources have a frequency independent spectrum. The final assumption is ergodicity for the involved stochastic processes. Under these assumptions, RIN is defined as :

$$\mathrm{RIN}(\omega) = \frac{S_P(\omega)}{\langle P(T) \rangle_T^2} \tag{2.34}$$

where $P(t)$ is the power at a time t, and S_P is the spectral density, given by:

$$S_P(\omega) = \int_{-\infty}^{+\infty} \langle\ \Delta P(t+\tau)\Delta P(t)\ \rangle \exp(-i\omega\tau) d\tau \tag{2.35}$$

where $\Delta P(t)$ is the deviation from the average. As such, the spectral density is the Fourier transform of the autocorrelation, ensuring that the power is conserved from the time domain to Fourier and that RIN can be analysed both ways, justified by the Wiener–Khinchin theorem for wide sense stationary processes [27].

RIN is best characterized in the frequency domain, as the methods to achieve it are readily available, with high dynamic range and spectra contain information about the sources mentioned above. The previously mentioned gain fluctuations are associated with relaxation oscillation frequencies. In the case of the Ti:Sa, the upper state lifetime of 3.2 μs is the main driver of such fluctuations, corresponding to a cut-off t 200-300kHz [28]. Cavity fluctuations are of mechanical nature. Their signature is visible up to a few kilohertz (kHz). Spontaneous emission fluctuations are purely quantum mechanical. In a semi-classical treatment, they are represented by white noise over the gain range. White noise is also associated with vacuum fluctuations, a purely quantum mechanical effect contributing over the whole spectrum, introduced in the set-up by optics such as the output coupler of the laser [29]. As such, vacuum fluctuations represent a lower threshold for the noise measurements in an optical

system, called the shot noise limit :

$$S_{\text{RIN}}^{\text{shot noise}} = \frac{2\hbar\omega}{P_{\text{avg}}} \tag{2.36}$$

While RIN is best characterized in the frequency domain, the background and random noise can also be meaningfully characterized in the time domain. By doing so, we can also define the notions of signal to noise ratio and signal to background ratio. The background in generation and detection of THz has two origins. The sources with a frequency dependant response in the RIN characterisation of the laser constitute the first origin. The second one is any other optical process happening simultaneously with the targeted optical processes in the set-up. In our case, it would include any other non-linear optical effect that is not DFG at the generation, and linear effects such as, but not limited to, scattering or back reflections from interfaces in the set up. In the measurements, the background, B, will appear as the mean value of the measurement before the signal. The random noise coming from the shot noise and any noise originating from the processing of the input photons is represented in the time domain by the standard deviation of the measurement before the signal, σ. With these definitions, we can define the signal-to-noise ratio (SNR) and signal-to-background ratio (SBR) in this text:

$$\begin{aligned} \text{SNR} &= \frac{S_{P2P}}{2\sigma\sqrt{\Delta f}} \\ \text{SBR} &= \frac{S_{P2P}}{B\sqrt{\Delta f}} \end{aligned} \tag{2.37}$$

where S_{P2P} is the signal peak-to-peak, Δf is the acquisition bandwidth, associated with the measurement. In this time domain picture, the sensitivity of our measurement is random noise. broadband character of white noise determines an upper bound on the SNR, for a given signal. Reaching a lower bound on the random noise is the way to optimize the retrieval of the signal. The importance of maximizing the SBR is felt on the electrical processing end. For a weak SBR, the dynamic range of the optoelectronic system is wasted for the reading of the background [30]. The lowest value effectively measured then is much higher than the lowest optical contribution, raising the lower bound on sensitivity. Low SBR also has implications in imaging, where it leads to lower visibility.

2.4 Theory of electronic methods

2.4.1 Lock-in detection

Lock-in detection is a signal processing technique aiming to drastically improve signal to noise ratio by exploiting previously known information about said signal. More specifically, information about the frequency at which the targeted signal is modulated is used to single it out against a noisy background. The instrument used to perform this task is called a lock-in amplifier. While initially done in an entirely analog way, newer systems combine analog and digital processing to reduce systematic errors and achieve better sensitivity.

Noisy background combined with targeted signal will be called input throughout this section. This input is required for the lock-in amplifier. A reference signal, which will be called reference from this point onward, can be locally generated on the lock-in amplifier, or given by an external source. The reference is divided, and an $\pi/2$ phase shift is applied to one of the products. The input is also split in two and each product is mixed with one product of the divided reference, yielding in-phase and out-of-phase components. This process is called down-mixing, or depending on the frequency of the reference, heterodyne/homodyne detection.

To in-phase and out-of-phase components, a low pass filter is applied, keeping only the targeted signal, which will be referred to as signal, from now on. Low pass filtering the signal effectively reduces noise by eliminating the noisy background.

Down-mixing followed by low pass filtering is known as demodulation. When producing an in-phase and out-of phase component, it is specifically known as dual phase demodulation, leading to recovery of about amplitude and phase of the signal. Dual phase demodulation can be better understood through a simple time and frequency domain mathematical derivation.

In the time domain, the signal S can be modeled as sinusoid:

$$S(t) = \sqrt{2}A\cos(\ \omega_S t + \Omega\ ) = \frac{A}{\sqrt{2}}(\exp[\ i(\omega_S t + \Omega)\ ] + \exp[\ -i(\omega_S t + \Omega)\ ]) \tag{2.38}$$

where Euler has been used, and ω_S is the frequency of the signal, Ω is the phase and A the amplitude. While sinusoid is not the only way of modulating a periodic signal, it is important to note that having only one harmonic, they introduce less errors in the demodulation process than other periodic waveforms.The reference is:

$$R(t) = \sqrt{2}\exp(-i\omega_R t) = \sqrt{2}[\ \cos(\omega_R t) - i\sin(\omega_R t)\ ] \tag{2.39}$$

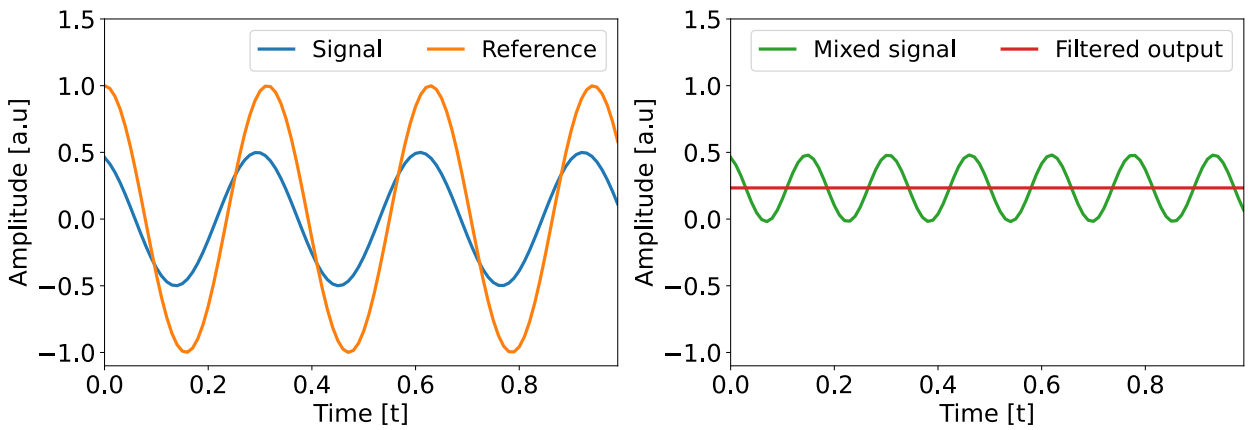

Figure 2.6 Time domain visualization of the effect of the lock-in amplifier. **Left :** Initial signal and reference, with different phases and amplitudes. **Right :** Signal after mixing with double frequency component and non zero mean. Filtered output takes out the higher frequency component.

where ω_R is the frequency of the reference. By mixing signal and reference, we obtain:

$$S(t)R(t) = A(\exp[\, i(\,(\omega_S - \omega_R)t + \Omega\,)\,] + \exp[\, -i(\,(\omega_S + \omega_R)t + \Omega\,)\,]) \tag{2.40}$$

In this equation, we have two terms. The first one is at low frequency, while the second is at much higher frequency, especially when $\omega_R = \omega_S$ (homodyne detection), in which case we have a DC term and frequency doubled term.

Low-pass filtering in the time domain is similar to averaging. The high frequency term averages out to zero, leaving :

$$S(t)R(t) = A(\exp[\, i(\,(\omega_S - \omega_R)t + \Omega\,)\,]) \approx A(\exp[\, i\Omega\,]) \tag{2.41}$$

where the approximation is made for the homodyne case.

By taking the real and imaginary parts, we obtain the in-phase and out of phase components :

$$\begin{aligned} X &= Re(\, S(t)R(t)\,) = A(\cos(\Omega)) \\ Y &= Im(\, S(t)R(t)\,) = A(\sin(\Omega)) \end{aligned} \tag{2.42}$$

Transition between time and frequency domain is handled by the usual Fourier transform.

In particular, after the mixing, we have:

$$Q_{in}(\omega) \xleftarrow{\mathcal{F}} S(t)R(t) \tag{2.43}$$

with Q_{in} the signal mixed with the reference and ω the frequency variable. The filtering process is mathematically simpler in the frequency domain, where it is described by:

$$Q_{out}(\omega) = H(\omega)Q_{in}(\omega) \tag{2.44}$$

where Q_{out} is the output of the filter and H is the frequency dependant response function associated with one filter. The most practical filter is the simple RC (resistance/capacitance) filter, whose response function is :

$$H(\omega) = \frac{1}{1 + i\omega\tau} \tag{2.45}$$

with $\tau = RC$ the time constant associated with the RC filter.

Of course, such a filter is far from an ideal "brick-wall" filter, whose response would be 0 outside of the bandwidth of the filter and 1 inside of it. Such a filter would be non-causal, as its impulse response would be infinite. To approximate such a filter, n RC filters can be used in series. Since the response from one filter is fed to the next one, the overall response is described by :

$$H_n(\omega) = \left(\frac{1}{1 + i\omega\tau}\right)^n \tag{2.46}$$

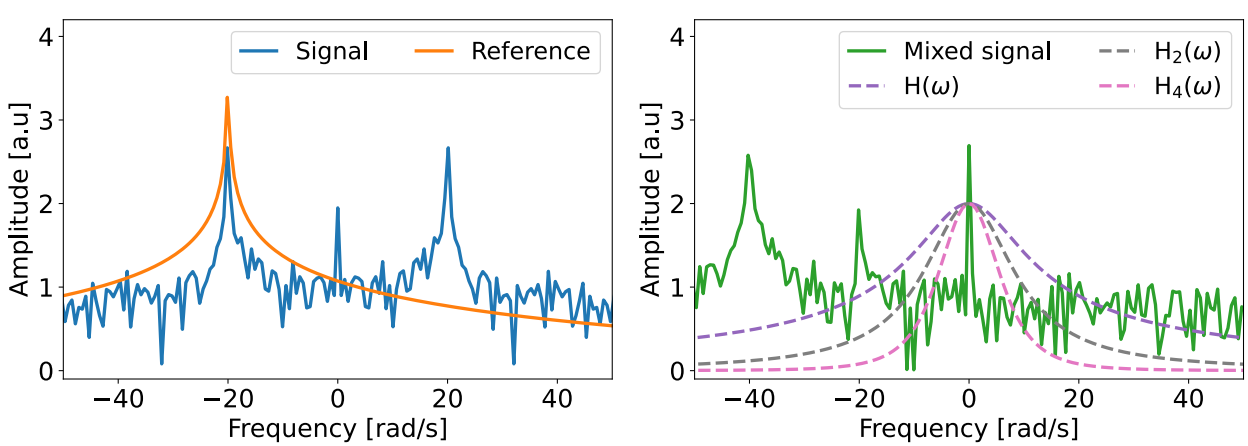

Figure 2.7 Frequency domain representation of demodulation. **Left :** Initial signal and reference fed to the lock-in. **Right :** Mixing "displaces" the signal, while increasing orders of the same RC filter block out more noise.

2.4.2 Boxcar averager

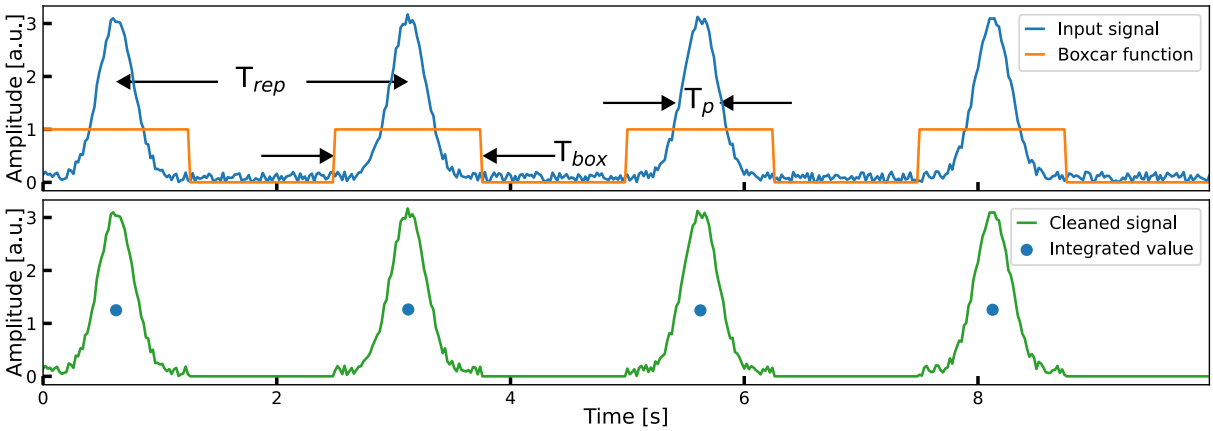

Figure 2.8 Representation of the boxcar basic principle. **Top :** Input signal and boxcar train. **Bottom :** Cleaned signal and integrated value within each boxcar window.

A boxcar averager is another tool used generally for SNR improvement. It is best used for measurements where the targeted signal is pulsed with a low duty cycle, which is the ratio of the pulse duration T_p by the period of the signal T_{rep} [31].

The working principle behind a boxcar averager is simple. Much like the lock-in amplifier, the boxcar averager requires a reference and an input signal. The reference is used to create a square wave going from 0 to 1 at its driving frequency. The period of time during which the value is equal to 1 is called the boxcar window, T_{box}. This square wave is called a boxcar train due to its shape. The input is then multiplied by the boxcar train, effectively discarding anything outside of the boxcar window. The input within each window is then integrated to produce one shot. The shots are then averaged over N cycles with a moving average filter, giving one point in the boxcar output. Figure2.8 shows how the integrated values are obtained from the input signal.

After providing the input and the reference to the boxcar, the user has three parameters to enhance SNR. The first one is the width of the boxcar window, the second one is its starting point and the final one is the averaging periods. The width of the boxcar window determines how much of the signal is retrieved, while doing the same for the noise at that point. The captured noise increases as $\sqrt{T_{box}}$ for white noise, while the increase in signal depends on its shape. The ideal way to optimize the width for an arbitrary shape is then to compare the SNR for different widths until the peak is reached. The starting point of the window is as important as the width, as it determines if any part of the signal is captured by the window.

Once the window has been set, the averaging periods increase SNR as $\sqrt{N}$ as discussed in the previous section.

In the specific use case of the RIN analysis, the goal is not the optimization of the SNR, but an aim for the highest available frequencies in the Fourier domain. It is entirely determined by the averaging periods, as the maximal frequency in the measurement is divided by N. This maximal frequency can further be limited by limit bandwidths in the set-up used for the measurement.

2.4.3 Double resonant circuit

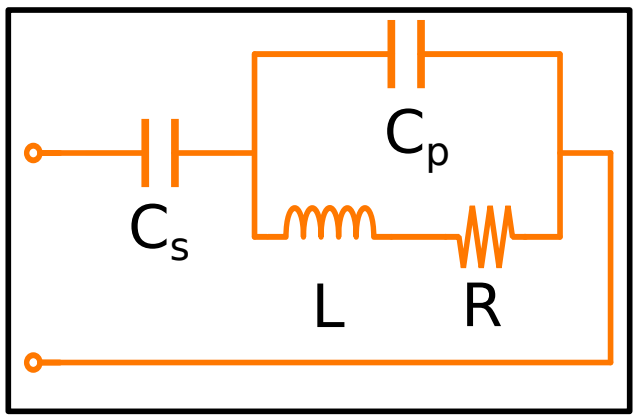

Figure 2.9 Schematic of the double resonant circuit. L: inductance, C_s: series capacitance, C_p: parallel capacitance, R: resistance

The polarization of the field radiated by the spintronic emitter depends on the orientation of the B field in which it is immersed. As such, the polarization can directly be modulated by modulation of the external B field. The previous sections motivate the need for high frequency modulation. One way of achieving high frequency modulation of a B field is by using a coil, which is effectively as simple resistance (R), inductance (L) and capacitance (C) circuit. In such systems, we have :

$$B(t) \propto I_L(t) \tag{2.47}$$

where $B(t)$ is the time varying B field and $I_L(t)$ is the time varying current going through the inductance. While the theory and implementation of a basic RLC circuit at lower frequency is straightforward, higher frequencies (hundreds of kilohertz) prove to be a challenge: at higher driving current frequencies, the impedance of the coil reaches values making it difficult to produce significant current through the inductance [32]. The poorly "driven" coil emits a weak B field, as per equation (2.47).

The impedance in a RLC circuit is given by:

$$\begin{aligned} Z_C &= \frac{-i}{\omega C} \\ Z_L &= R + i\omega L \end{aligned} \tag{2.48}$$

where ω is the frequency of the driving current, Z_C is the impedance of the capacitance and Z_L is that of the inductance. In this case, we have included the resistance in the inductance's impedance. We add to these formulas the principle of equivalent impedance in a circuit : the equivalent impedance of elements in series is the sum of the elements individual impedance, while that of elements in parallel is the inverse of the sum of the elements individual impedance. The frequency at which the coil operates is the resonance frequency, ω_0. At that frequency, the imaginary part of the equivalent impedance of the circuit is null. We can exploit the negative contribution of a capacitance to balance the impedance of a RLC circuit by putting the circuit in series with a suitable capacitor. This impedance matched circuit is called a double resonant circuit. At the resonance of such a circuit, we expect to have:

$$\begin{aligned} \mathrm{Img}(Z) &= 0 \\ \Rightarrow \mathrm{Img}(Z_p) + \mathrm{Img}(Z_s) &= 0 \end{aligned} \tag{2.49}$$

where Z is the total impedance, Z_p is the impedance of the RLC circuit and Z_s is that of the external capacitance. As we aim for high current in the coil, we need to keep R at a minimum. We can then consider it negligible for the next steps of this mathematical derivation. We then have :

$$\begin{aligned} \mathrm{Img}(Z_p) &= \frac{1}{\omega C_p - \frac{1}{\omega L}} \\ \mathrm{Img}(Z_s) &= \frac{1}{\omega C_s} \end{aligned} \tag{2.50}$$

which still holds true at ω_0. By substituting these values in eq.(2.49), we find the resonance frequency to be :

$$\Rightarrow \omega_0 = \frac{1}{\sqrt{L(C_s + C_p)}} \tag{2.51}$$

For simplicity, we decided to focus on the particular case where the capacitance of the RLC circuit and the external capacitance are the same, $C_s = C_p = C$. By applying Kirchoff's law

of tension in a circuit on the RLC circuit, we find :

$$\begin{aligned} U_L + U_C = 0 \\ \Rightarrow I_L \times Z_L + I_C \times Z_C = 0 \Rightarrow I_L = \frac{I_C}{\omega_0^2 LC} = 2I_C \end{aligned} \tag{2.52}$$

where I_C is the current through the capacitor, U_L and U_C are, respectively, the tension through the inductance and the capacitance. We can apply Kirchoff's law of current to find the relationship between the driving current and the current through the inductance:

$$\begin{aligned} I_S + I_C = I_L \\ \Rightarrow I_L = 2I_S \end{aligned} \tag{2.53}$$

we then see that driving current is doubled when it gets to the coil. The double resonant circuit is expected to produce a strong B field at high frequencies, based on the theory behind the functioning of such a circuit.

2.5 Literature review

The invention of the laser opened the door to a non-linear approach of light-matter interactions. Harnessing the advances made in the past few decades in electronics and non-linear optics for high performance applications in spectroscopy is the aim of the text. As such, we will do an overview of the progress achieved in coherent generation and detection of terahertz on the facets most important to this use case, that is bandwidth, frequency range and noise performance. This overview will progress chronologically when it comes to improvements made in OR, EOS and spintronic emission of THz, around which this project revolves, after what a quick presentation of other techniques is given to accurately assess the benchmarks in terahertz time-domain spectroscopy.

In the two years following the invention of the laser in 1960 [33], SHG [34] and OR [35] were observed and described. In the case of OR, it was done through KH_2PO_4 and KD_2PO_4 in 1962. As mentioned in section 2.1.1, this was the particular case for which the input frequencies are exactly the same, due in part to the monochromatic nature of the source. The generated field was simply a DC voltage. The first use of DFG, colloquially called OR, for THz generation was done through quartz to produce radiation around 3THz from a source emitting from 1059nm to 1073nm in 1965 [36]. Phase matching was done and produced radiation in both ordinary and extraordinary polarizations. At the time, detectors had yet to be made coherent, and the bandwidth of the output could not characterized.

The next important milestone was the presentation of a new method of coherent detection with a time resolution on the picosecond scale, in 1982 [37]. Advances in laser performances meant that colliding pulse mode-locked (CPM) dye lasers with repetition rates of 100MHz and pulse duration of 120fs were available. With such an instrument, EOS was first demonstrated as method of coherent detection of an ultrafast electric signal in lithium niobate. The signal source was modulated with an optical chopper, operating at 1kHz and used in conjunction with a lock-in detection system. While the duration of the CPM generated pulse was 120fs, the resolution was limited by the traversal time through the $LiNbO_3$ crystal. In a phase matched configuration, this traversal time was 3.6ps. The lock-in detection at kHz frequency produced a sensitivity of less than 50 μV. It was acknowledged that this value was also dependant on the averaging done through the lock-in detection process, but the number of scans per averaging was never mentioned. In a subsequent article by the same team published in 1986 [14], a 40dB improvement in sensitivity is suggested as a consequence of moving from kHz modulators to acousto/electrooptic modulators in the radio frequency(RF) domain.

EOS was immediately recognised as a means of THz detection and the first detection of a single cycle THz waveform was realized in 1984 [38]. Once again, a CPM ring dye laser was used. With a duration of 100fs and a repetition rate of 150MHz, OR was done in lithium tantalate. Lithium tantalate was also used as the EO crystal. In this particular experiment, the impulse beam was separated in two, one part used for the THz generation and the other for the probing, a configuration that is also exploited in our current set-up. In this configuration, the temporal resolution is entirely fixed by the duration of the probe in the EO crystal. The Fourier transform of the measured waveform showed a peak at 1.2THz, with a bandwidth, at 10% of the peak, expanding from DC to 3.6THz. While noise performance was not discussed in that experiment, it was the first instance of coherent generation and detection of THz and the implications for spectroscopy were noted : it marks the beginning of time domain terahertz spectroscopy.

The four decades separating us from that point saw a clear intent to improve on this already functional technique. This intent bore fruits on different fronts : time resolution, noise performance, usable bandwidth and ease of use. While mode-locked lasers readily offered fs resolution, which was beyond necessary given the materials used at the time, it was clear that the repetition rate could better be exploited in the lock-in detection scheme to improve noise performance. Indeed, modulation at RF frequencies, commensurate with the repetition frequency of the mode-locked lasers, would automatically cut out the noise associated with low frequencies, such as 1/f noise or mechanical noise, as proposed by the EOS inventors. The obstacle at the time was the inferior performance of RF lock-in amplifiers compared to the acoustic lock-in amplifiers already used: RF amplifiers were quoted to be up to 100

times noisier than their acoustic counterparts [39]. The first solution to this issue in the EOS community was the use of a synchronous RF mixer system for RF modulation of the source and mixing of the dual detectors signals [39]. The difference in RF frequencies for the two detectors would be 100kHz, where the lock-in amplifier would work, with a time constant of 100ms. With this method, in 1990, and no further averaging, measurements where done with a sensitivity of 270μV, two orders of magnitude lower than what they obtained by direct use of a 100kHz lock-in detection method. The set-up in that experiment was also a CPM laser with a repetition rate of 100MHz, delivering 70fs pulses. It is true that the sensitivity obtained by the EOS inventors was lower, but no information was disclosed concerning the number of scans averaged. The sensitivity value obtained through this mixer based EOS system set a new benchmark. In 1989, digital lock-in amplifiers reaching higher frequencies with better performances than their analog counterparts were proposed [40]. Their adoption throughout the nineties led to the final frontier in EOS with regards to sensitivity. Indeed, by 1996, EOS detection was done with a mode-locked Ti:Sa with a 76MHz repetition rate, a pulse duration of 160fs, at a chopping frequency of 95kHz. In such a system, 3V/cm/$\sqrt{\text{Hz}}$ sensitivity was achieved with 10 scans average, putting it 29dB (1000times) above the shot noise limit [41]. This floor was lowered to 5 times the shot noise in 1998 [42]. In this experiment, the lock-in detection was done at an difference frequency between the 0.9MHz used to modulate the pump through an acoustooptic modulator and the 0.9007MHz frequency mixed with the detected signal. The use of this mixing method is proof of the experimental difficulty of modulation at frequencies approaching RF. For a noise floor 5 times higher than the shot noise, a shot noise measurement can be achieved by averaging 25 measurements. At the turn of the century, such high frequency modulation schemes, associated with adequate averaging made shot noise limited measurements common for the EOS detection of THz [43].

Another crucial part of the development of the THz optical toolkit was the quest for suitable materials. Suitable materials are evaluated through their non-linear coefficients, which determines the efficiency of the process. They are also evaluated by the position of their phonon resonances, as they can cause absorption/reflection at those frequencies, creating "gaps" in the spectrum. The final criterion is their damage threshold, determining how well they resist to the intense radiation required for $\chi^{(2)}$. Non-centrosymmetric materials are required for $\chi^{(2)}$ processes. Among all materials satisfying this requirement, three main categories of materials have been investigated : semiconductors, ferroelectric materials and organic materials. In this text, we will limit ourselves to ZnTe and GaSe, two II-VI semiconductors used in this project. They respectively have their lowest transverse optical phonon frequencies at 5.3THz and 6.4THz, and lowest longitudinal optical phonon frequencies at 6.2THz and 7.6THz: these Reststrahlen bands are "gaps" in the emission/detection spectra of these ma-

terials [44] [45]. ZnTe and GaSe also have a damage threshold in the near infrared on the order of a hundred GW/cm^2 [46]. Finally, GaSe is an extremely birefregent crystal. It is then possible to achieve phase matching and increase the effective interaction length, leading to higher efficiency of the process under consideration and tunability of the emission/detection range. Phase matched generation of THz in GaSe has been shown to produce single cycle terahertz radiation with a peak at 26THz and a full width at half maximum of 16THz, while phase matched detection has been shown as a reliable way of detecting frequencies up to 100THz [47]. ZnTe has also been shown to detect frequencies up to 100THz, but with additional "gaps" due to a mismatch of the propagation speed of the THz and probe beam in the crystal, a phenomenon called group velocity mismatch [47]. ZnTe has been used to produce THz radiation peaking at 10THz and extending to up to 40THz [43].

Phase matched OR and EOS permitted higher SNR and bandwidth for the THz toolkit in the early 2000s. Still the Reststrahlen band of the semiconductors used meant a difficult access to the full bandwidth, only possible through use of multiple crystals with overlapping bandwidths. While better understanding of the phenomena causing the band can help fabricate materials with different properties, one promising alternative was presented in the 2010s: spintronic emitters. They have been shown to emit without gaps over the DC to 18THz range with the possibility to extend to 30THz [18]. Emission over this range has been shown to have similar intensity as OR. Another advantage is that 10kHz modulation of the THz radiation has been done through modulation of the external magnetic field in which it immersed [48]. That way, no additional path length is required, contrary to EOM or AOM, and there is a possibility of reaching much higher frequencies of sinusoidal modulation, which is not possible with optical choppers. The current upper limit for modulation of spintronic emission is still 10kHz, with a suggestion that it can be pushed up to 100kHz, over which the functioning of the emitter is not guaranteed.

OR, EOS and spintronic emission face competition with a few other techniques one of which will be succinctly presented here. The most popular competitor for generation and detection of THz radiation are photoconductive antenna (PCA). In that scenario, an ultrafast laser creates free carriers in a semiconductor, which are then accelerated by the bias field of the antenna thereby generating THz radiation [49]. PCA sampling for detection is done by gating the antenna with the same ultrafast optical beam used for generation. The THz transient incoming on the gated antenna produces a photocurrent that is linearly dependant on the THz transient field. The bandwidth in this method is limited by the carrier lifetimes in the material used [50]. Generation has been done under 10THz while detection has been achieved up to 40THz with high sensitivity [51] [50].

We have now established that EOS offers high bandwidth detection of THz radiation with a gap a the Reststrahlen band, while OR and spintronic emission permit generation of strong THz over the DC to mid infrared (MIR) range. The sensitivity of the detection is heightened by modulation that is high frequency and shot noise limited for OR, while still in the few kHz regime for spintronic emitters. They evolved over time to become great tools for time domain THz spectroscopy, in which they are joined by PCA generation and detection. With this knowledge of the state of the art in generation and detection of THz and the path taken to get to this point, the aim of this text is to understand how to bridge the gap in the sensitivity of the detection scheme when using a spintronic emitter as a source.

CHAPTER 3 RELATIVE INTENSITY NOISE CHARACTERIZATION

Shot noise limited detection has been achieved through modulation of the signal in a pump probe experimental set-up using only one mode-locked fs laser as the source for both arms. Noise transfer theory shows that noise is "carried" over from one element to the next, by addition in the frequency domain. Keeping this in mind, it is crucial to know the frequency range at which the contribution from the laser is minimal if we are to reach shot noise limited detection in a set-up where spintronic emission is the THz generation method. Finding this frequency range is done by RIN characterisation of the laser source. It was stated in section 2.2 that modulation of the output polarization of the laser is done by modulation of the external magnetic field in which it is immersed. Once the modulation frequency is found, we will propose a method of modulating the external B field at that frequency and quantify the expected improvement compared to modulation of the signal at lower frequencies. The estimated improvement from the RIN measurement will be compared to the actual THz measurements, testing the hypothesis whether the total noise of the THz measurement is dominated by the source noise.

3.1 Ti:Sapphire RIN performance

3.1.1 Laser system

The laser source used throughout this project is a home assembled titanium sapphire (Ti:Sa) laser. It is pumped by a diode-pumped solid state (DPSS) laser from Laser Quantum (Finesse Pure). This pump laser is a frequency doubled neodymium doped yttrium aluminum garnet (Nd:YAG) emitting at 532nm. It is low noise with a root mean square noise (σ_{DPSS}) less than 0.02% and produces a TEM_{00} spatial mode with a horizontal polarization. This first stage serves as a pump to a broadband gain medium which is sapphire crystal doped with trivalent ions of titanium. The $\chi^{(3)}$ nonlinear response of the gain medium is also used to initiate passive mode-locking mechanism through the Kerr-lensing effect, shifting from continuous wave operation towards pulsed operation. The Ti:Sa crystal is in a 2.35m cavity in an "γ" configuration, leading to a repetition rate of 63.67MHz. The spectral dispersion inside the cavity is compensated by dielectric chirped mirrors. The wedged output coupler lets out a Fourier limited 10fs pulse, with a full-width at half maximum (FWHM) bandwidth of 120nm centered at 800nm and a mean power of 900mW when the pump laser is set at 7.7W. The angular dispersion added by the output coupler is compensated by another wedged dispersive

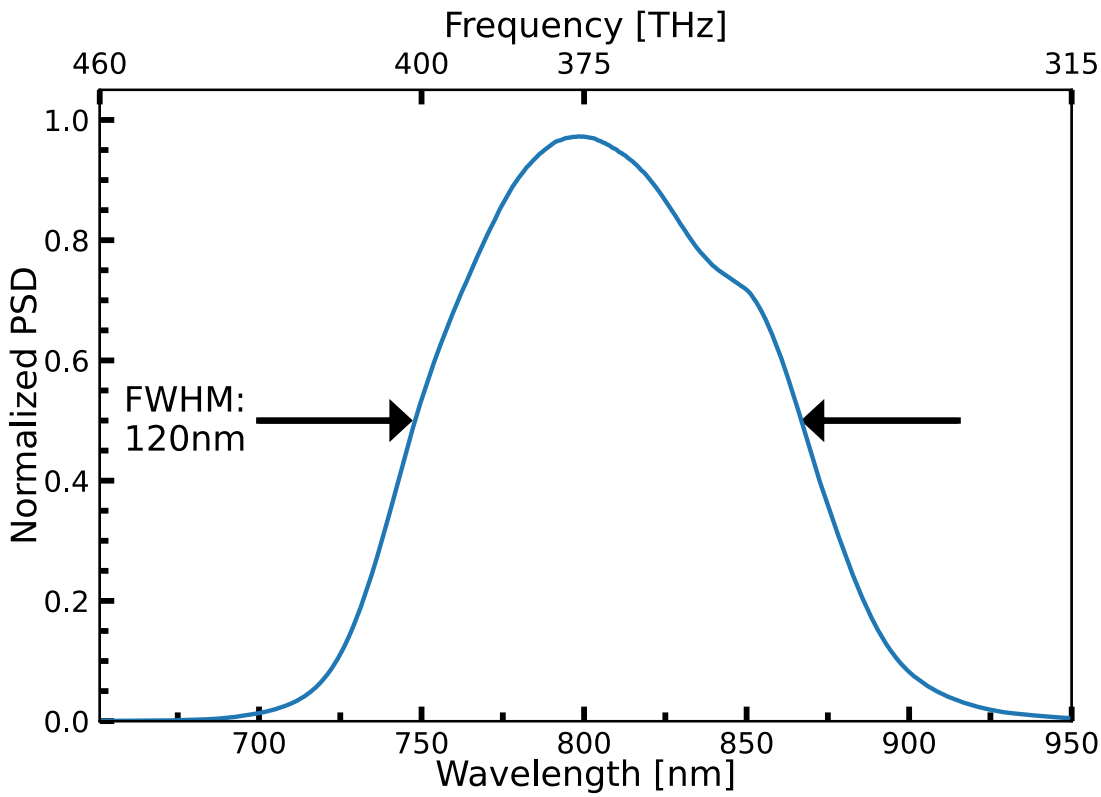

Figure 3.1 Spectral output from the mode-locked Ti:Sa laser source.

element. The added spectral dispersion, as well as the dispersion of the optics inside the set-up before the GX crystal is precompensated by a pair of chirped mirrors outside of the cavity.

3.1.2 Noise characterization set-up

As seen in equation 2.35, RIN characterisation in the frequency domain begins with a time measurement of the power. In this section the set-up for the time measurement is described.

The power is measured by illuminating a reverse biased silicon detector (Thorlabs DET10A) with a 1ns rise time and responsivity of 0.4A/W at the central frequency. To fit the 1mm diameter active area, the laser beam is passed through a lens, before which it is attenuated to keep the detector in the linear response regime. Neutral density filters are used to reduce the power of the laser.

The recording of the measurement is done with a boxcar averager (Zurich Instruments UHFLI), sampling at 1.8GSa/s with a maximal transferable bandwidth of 1MHz. The Nyquist-

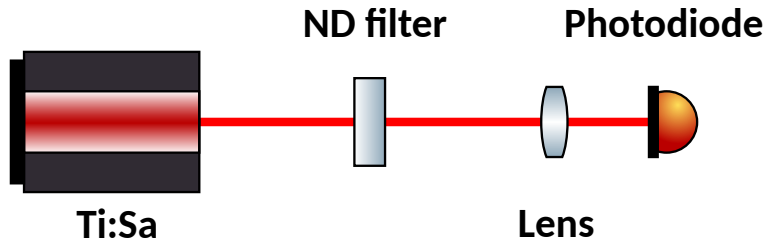

Figure 3.2 Relative intensity noise characterisation optical set-up. The photodiode is connected to the boxcar system.

Shannon sampling theorem tells us that any signal with a maximal frequency f_m can only be properly described with a sampling frequency of $2f_m$. Considering the 63.67MHz repetition rate of the laser, the maximal transferable bandwidth constitutes a "bottleneck" for our measurement. The averaging on the boxcar is chosen to reduce the bandwidth to fit into this upper limit. As such, each point transmitted is the average of 64 successive boxcar shots and any information above 1MHz is averaged out. The boxcar window is opened for 5ns, which is commensurate with the detector's response to one pulse, as confirmed by a periodic wave analyzer. The boxcar has two input impedance settings that also affect its AC operation : a 50Ω termination that sets a 320kHz high-pass filter and a 1MΩ termination associated with a 80Hz high pass filter. For our purposes, the main measurement is done with the AC operation, with a 1MHz termination. By filtering out the DC component, the full 21-bit resolution of the boxcar averager is dedicated to the lowest possible range of the boxcar, ±10mV. The resolution then is 9.53nV. The other measurement is done without the AC operation, informing us of the mean power reaching the detector. The measurements are done at the repetition rate of the laser until the memory of the boxcar averager is full, which is up to 5s.

3.1.3 RIN performance and improvement benchmark

Characterisation in the frequency domain gives us better understanding of the source of the noise, it is however reliant on processing, and inspection of data at different steps gives greater confidence in the final results, while giving insight into what can be expected. The time domain measurements are presented here in two ways. We will begin with a brief discussion concerning the time evolution of the boxcar measurements before diving into an analysis of the noise in the frequency domain.

In figure 3.3, the impact of the 80 Hz high pass filter is clearly visible. Without it, the measurement contains elements at low frequencies, responsible for the overall variations of

the trace. In the filtered case, the trace is flat overall, which can be expected. The overall noise performance of the laser can be quantified by the RIN integrated from $1/t_{max} = 0.22$Hz to 1MHz. In the time domain, this value is simply the ratio of the variance of the power to the mean power, σ/μ=0.047%, which shows that the laser is noisier than the pump laser, which is expected. The integrated RIN from 80Hz to 1MHz in this case is 0.0042%. This reduction is also in line with the theory: most of the noise is at lower frequency where pink noise dominates.

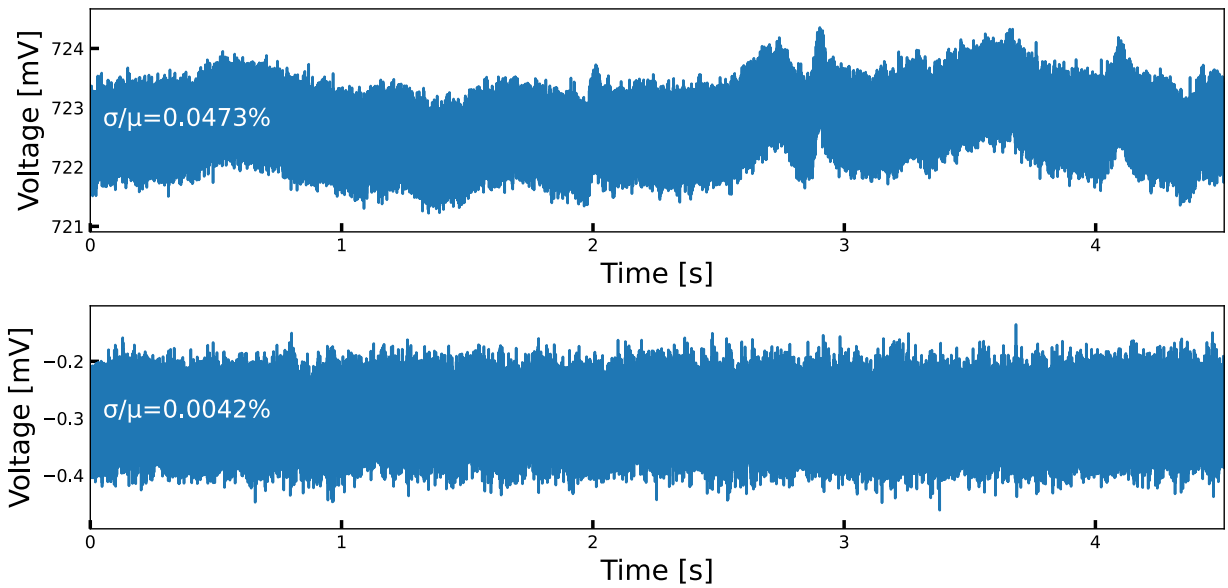

Figure 3.3 Time domain representation of the boxcar output. **Top :** Unfiltered. **Bottom :** 80Hz electrical high-pass filter applied to the output.

Another way to visualize the noise performance in the time domain is by using histograms. The shape of a histogram can help in determining the source of the noise, if the timescale of the measurement is commensurate with the noise source. For instance, a white noise source in the frequency domain, as the shot noise, will have a time trace that is described by a gaussian statistical distribution, when presented in the form of a histogram. By the central limit theorem, a gaussian distribution can also serve as proof of sufficient sampling of the signal. The graphs shown in figure 3.4 are obtained from the same measurements as the time traces already presented. The time traces are acquired over a certain time, whose inverse determines the resolution of the measurement in the frequency domain. The time elapsed between the measurement of two successive shots determines the bandwidth of the measurement, according to a similar inverse relation. This necessarily implies that the bandwidth of the measurement can be digitally reduced through averaging of successive

shots, which digitally increases the time between them. By averaging ten, then a hundred successive shots, the bandwidth is reduced and some features are exacerbated in the graphs shown. It is clear that the full 0.22Hz-1MHz bandwidth measurement is not gaussian. The histograms up to 100kHz and 10kHz make the skewness of the distribution more apparent, as seen by comparison of the top row in figure 3.4 with the gaussian distribution in the bottom row, obtained from the 80Hz high pass filtered measurement. It indicates that low frequency components are responsible for this skewness. The skewness in this case can be attributed to the shortness of the measurement with regards to the timescales of the sources, in other words the noise cannot be treated as time stationary for some (low-frequency) components. Events slower than 80Hz are dominating the shape, but 4.5s is not enough time for those random events to stabilize around a central value around which a gaussian would have been observed. On the other hand, the high-pass filtered distributions show that enough points have beeen collected for the phenomena we want to describe, as proven by the consistent gaussian shape, regardless of the bandwidth after averaging.

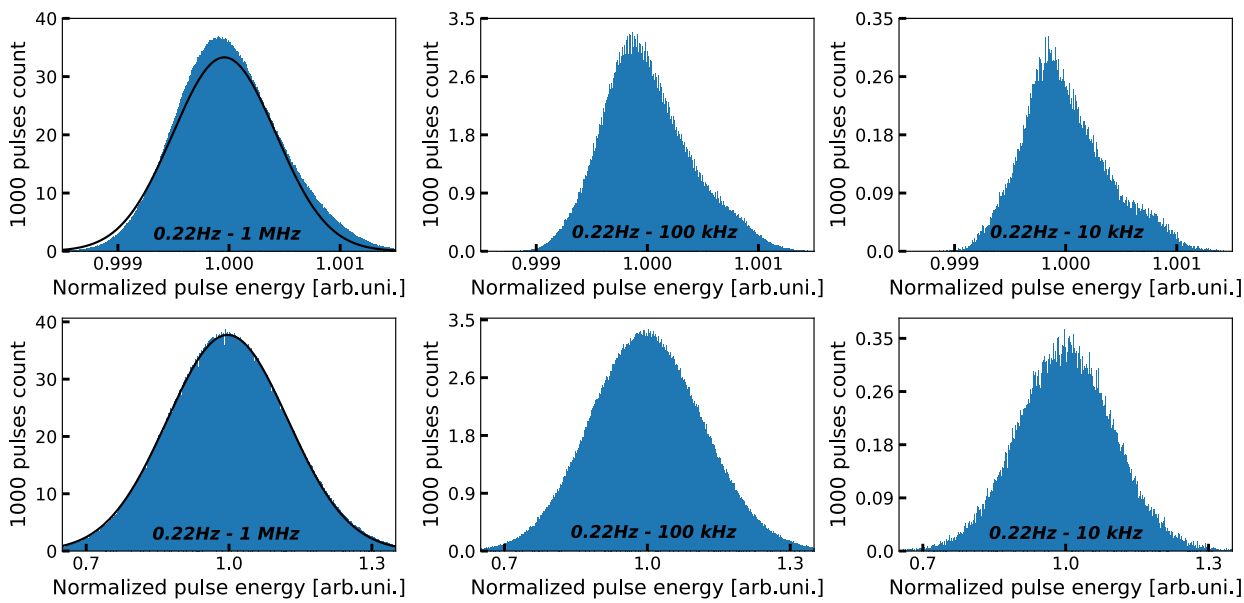

Figure 3.4 Distribution of the boxcar output around the mean value with different averaging bandwidths. Gaussian fit done on the first histogram for reference. **Top :** Unfiltered output. **Bottom :** 80Hz electrical high-pass filter applied to the output.

The next step in our noise analysis is the processing of the measurement to obtain the PSD. As indicated in section 2.3, the processing is done by subtracting the mean from the time measurement, after which a Fourier transform is applied to the obtained trace. To avoid seeing the effect of the boxcar step shape in the frequency domain, a Hanning window is

applied to the trace. The obtained Fourier transform is multiplied by its conjugate to produce the spectrum. The spectrum is then normalized to the square of trace average obtained with the boxcar measurements performed with the DC input, as mentioned above. It is then divided by the bandwidth of the measurement. The final step is applying a Savitsky-Golay filter, which makes the data easier to visualize on a logarithmic scale. We obtain figure 3.5 by this method. The unfiltered (blue) and filtered (orange) plots show the noise decreasing with increasing frequency, as expected. They eventually reach a plateau at frequencies above 100kHz. The full bandwidth measurement looks featureless from 10Hz all the way to a few hundred kilohertz, where we can see a few spikes. The absence of any features, for example, due to isolated low-frequency vibrations of activity mirrors (see section 2.3), is indicative that the measurement is not representative of the actual performance of the laser. The high floor reached is another indicator that the measurement is not representative and hints at a limitation imposed by the resolution of the electronic system. To confirm this hypothesis, we determine this resolution floor, as the minimal measurable value given the scale (alternatively called "range") of the measurement :

$$10 * \log_{10}\left(\frac{\text{Range}}{2^{21}}\frac{1}{\overline{V}^2}\right) \approx -124\text{dB} \tag{3.1}$$

This calculation shows that the plateau reached is indeed the resolution floor imposed by the boxcar system as seen in figure 3.5. It is clear that the full bandwidth measurement is not suited for the RIN characterization as the floor is raised and information is lost. To overcome this limit, the HPF was applied, taking out the DC component of the measurement and reducing the range as a consequence. The PSD obtained with the HPF applied is shown in figure 3.6. This figure shows the Savitzky-Golay filtered measurement with (orange) and without (blue) the HPF applied. It also shows the PSD of the photodiode background, which has been normalized using the same average value as the blue and orange plots. The two new graphs still show decreasing of the noise with increasing frequency, as expected. The presence of broad features in the HP filtered signal, up to 20kHz, is also expected and confirms that the resolution was the limiting factor in the previous measurement. At higher frequencies, some spikes are also observable in the HP filtered PSD and the photodiode background, the highest of which are also visible in the full bandwidth PSD.

Since applying a HP filter made the expected features apparent and lowered the floor towards an expected level, the high floor can be attributed to the resolution of the measurement set-up. Without the filter, the measurement has a high value for the mean, and the range of the measurement is set at ±1V. By taking out the lower frequency components, the range becomes ±10mV. The set-up is able to measure shot-noise only if the resolution floor is

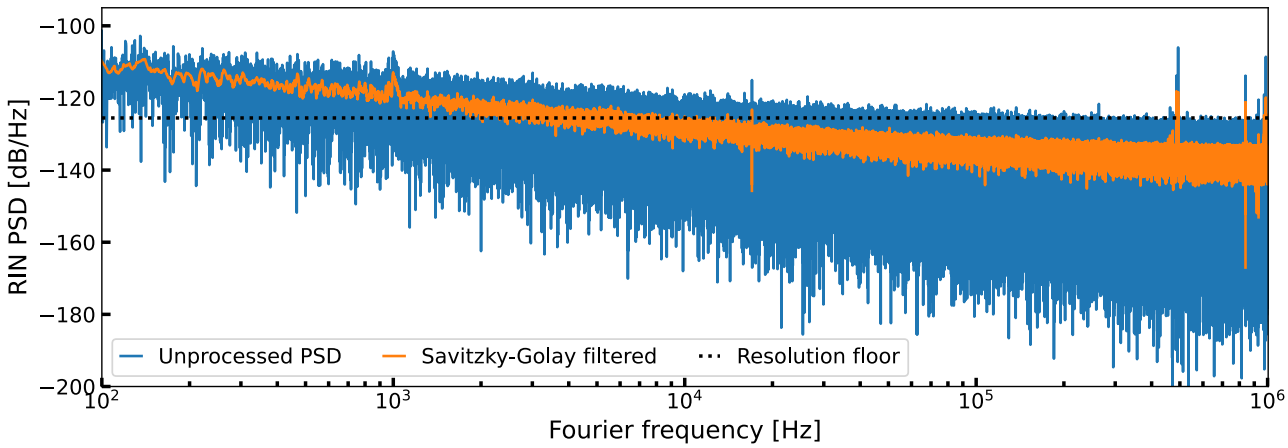

Figure 3.5 Power spectral density (PSD) of the unfiltered Ti:Sa output, from 100Hz to 1MHz. The "plateau" reached at high frequencies is "carried" by the resolution limit of the experiment.

lower than the shot-noise floor. With the new range, the noise floor becomes approximately -164dB. In comparison, the expected shot-noise floor is at -157dB, obtained using equation 2.36 for a central wavelength of 800nm and the average power of the laser incident on the photodiode (2.6mV). The HP filtered measurement is then sensitive enough.

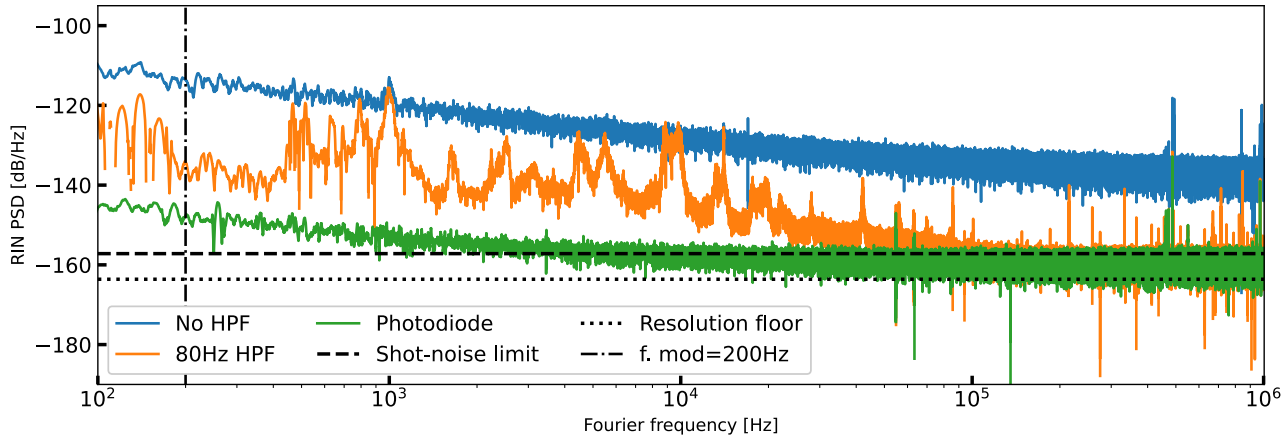

Figure 3.6 PSD of the photodiode and the Ti:Sa, with and without a 80Hz filter applied. The resolution floor is lowered by the filter, revealing features invisible in the unfiltered case, and reaching the shot-noise limited plateau at high frequencies.

With the Savitsky-Golay filter, peaks below 20kHz are now clearly observable. Those can be

associated with audible noise, originating from the water cooling system used, as well as any other audible noise in the vicinity of the laser. To those sources, we can also add vibrations inside the laser box that also contribute to noise in this range, such as the eigenfrequencies of mirror vibrations in the laser cavity. We can see that the filtered measurement reaches a floor around 160kHz. This floor has contributions from the laser itself, as well as the photodiode background, as it is used for the measurement. The measurement being within 5dB of the expected shot-noise with this added electrical noise from the photodiode, along with the absence of other features and the lower resolution floor, we conclude that the noise from the Ti:Sa is shot noise limited at those near RF frequencies. At those frequencies, we can also see spikes in the PSD that are not present in the photodiode background. Those spikes, e.g the one at 980kHz, can be attributed to the high current power supply required for the DPSS.

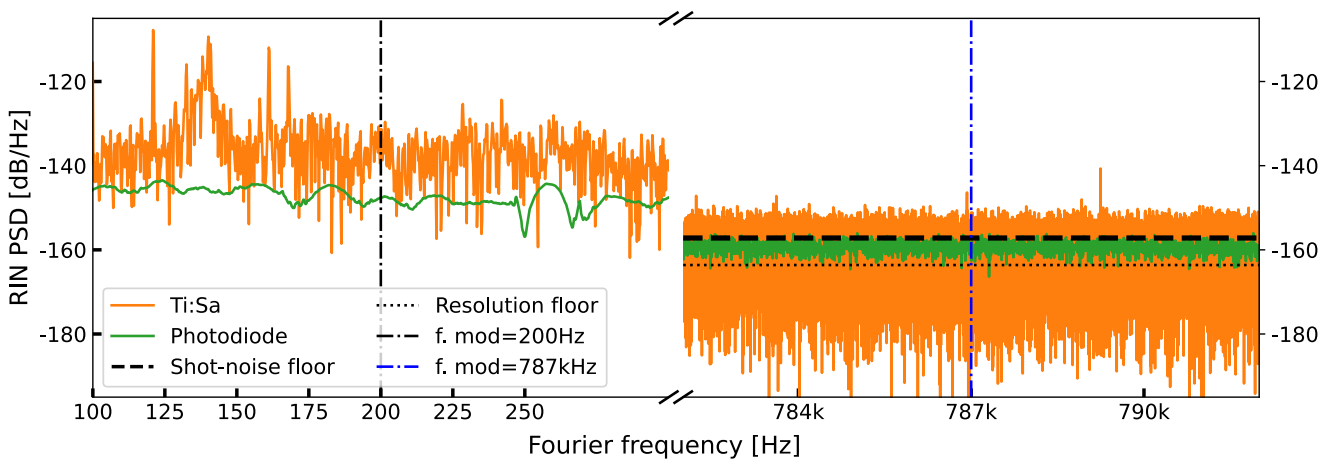

Figure 3.7 PSD of the filtered Ti:Sa and the photodiode outputs, showing the two modulation frequencies targeted in the text. This work uses two common modulation frequencies (see section 4) at 200 Hz and 787kHz, shown by respective vertical lines for reference.

With figure 3.7, we can make the choice for the modulation frequencies that can provide us shot-noise limited response. As a reminder, in the case of spintronic emitters, RIN is the dominant source of noise, hence figure 3.7 informs our design for the external magnetic field modulation to be at frequencies higher than 200kHz, ideally around 700-800 kHz where RIN of our Ti:Sa is shot-noise limited. We will revisit these assertions when we compare measurements of THz noise at different modulation frequencies and analyze their scaling in reference to the RIN noise performance. The other modulation frequency we use is f_{OC}=200Hz, dictated by the optical chopper available to us currently. The expected improvement is then the ratio between the noise picked up by a bandpass filter of the same width used a the two fre-

quencies of interest. As shown below, the external magnetic field is produced by a resonantly driven pair of Helmholtz coils, with their resonant frequency determined to be f_{HC}=787kHz (see section 3.2.1). The width of the bandpass filter is determined by the order of the RC filter we use, which is 3 and the time constant τ=100ms in our experiments. The bandwidth to consider is determined, for dynamic measurements, to be $0.081/\tau$=0.81Hz$\equiv$ f_{3dB}. The expected improvement is then :

$$\frac{i\mathrm{RIN}_{OC}}{i\mathrm{RIN}_{HC}} = \frac{\sqrt{\int_{f_{OC}-f_{3dB}/2}^{f_{OC}+f_{3dB}/2} S_P(f)df}}{\sqrt{\int_{f_{HC}-f_{3dB}/2}^{f_{HC}+f_{3dB}/2} S_P(f)df}} \approx 20 \tag{3.2}$$

The peak strength of the field is flipped around 0 through polarization modulation with the Helmholtz coil. Compared to the intensity based modulation of an optical chopper, going from the peak strength of the field to 0, polarization switching introduces a further factor of 2. This means that a total reduction of 40 is expected when it comes to measurement of the noise in the time domain, more specifically a reduction of the standard deviation of the measurement before the signal, σ. This is an enormous reduction factor, since for a normally distributed noise model this assumes that similar SNR can be achieved at higher modulation frequency in a $40^2 = 1600$ times shorter data taking time interval!

3.2 Negative delay electrooptic readout

To reach the shot noise limited sensitivity, modulation in the EOS set-up is done by use of a Helmholtz coil. In this section, a schematic of the EOS setup is given with a full description of the coil. A full presentation of the EOS set up is done in the next chapter. The results on the noise in the time-domain are also presented and discussed here.

3.2.1 EOS noise characterization set-up

The EOS set-up is a pump-probe scheme with the TI:Sa as sole source for the pump and probe beams. After splitting of the input pulse, the modulation of the signal is done in the pump arm of the set-up. An in depth description of the EOS set-up is done in the next chapter, here a summarizing presentation emphasizes the modulation methods for the spintronic emitted THz. With the spintronic emitter as THz source, two modulation schemes were used: an optical chopper at $f_{mod} = 200$ Hz and a Helmholz coil pair driven at $f_{mod} =$ 787kHz. The initial method was through the use of an optical chopper set at 200Hz, with a DC magnetic field of 20mT at the position of the spintronic emitter, which is a tri-layer of

W|CoFeB|Pt ($2\,nm|1.8\,nm|2\,nm$) in this thesis.

Figure 3.8 Picture of the prototype double resonant Helmholtz coil.

The new modulation scheme is done using two double resonant electromagnets to make a Helmholtz coil, shown in figure 3.8. Each magnet is built using gauge #38 Litz wire, made of 100 copper strands with a 0.1mm diameter. Litz wire was chosen to reduce skin effect that would have otherwise caused additional losses in the coil. The wire has been used to make 8 turns of 1.5cm diameter for each electromagnet, with only one layer to avoid parasitic inter-layer capacitance. While more turns would increase the output field, the driving voltage required would also increase. The diameter has been kept to 1.5cm to fit inside the EOS set-up. The electromagnets are 13mm apart, enough to hold the spintronic sample. This gives a Helmholtz coil with an inductance of L=2.0448μH. In the configuration described in section 2.4.3, the capacitor used is rated for high voltage (more than 1kV) and C=10nF. The measured resistance of the coil is R=229mΩ. The double resonant Helmholtz coil operates

at 787kHz, as confirmed by an impedance analyzer. The coil is driven by waveform amplifier (Accel Instruments TS250-0) whose input is produced by a waveform generator (RIGOL DG1022). The magnetic field depends linearly on the input voltage, which can be modified on the waveform generator. At the center of the coil, the peak magnetic field is B=254μT, obtained with a voltage of 3.1V_{P2P} on the waveform generator. This value is 40 times lower compared to the field produced by the other modulation scheme. It should be pointed out that high amplitude of the modulated B-field is hard to achieve due to large electric power requirements and will be considered for implementation if the current coil proves successful. The pump and probe beams are recombined before the EO crystal, after which they pass through an ellipsometric set-up with a balanced photodetector. The electrical connections of the probe-arm detection device are shielded in order to avoid direct pick up of the driving RF field, which otherwise introduces a large offset in the lock-in processed data. For the noise performance, the set-up has been used with and without the spintronic emitter in the pump arm. The EOS crystal used was a 500μm ZnTe crystal with a <110> crystalline orientation.

3.2.2 Noise performance

The time domain noise performance has been characterized in three ways. First a comparison between the low and high frequency modulation schemes' performances is done with the emitter in place. The second comparison is the same, with the pump arm blocked. Then a comparison of the noise performance at different input voltages on the waveform generator is done, at high frequency, with the emitter in place.

The main result is shown in figure 3.9. Comparison of the distribution of the EO readouts at negative delay. For this comparison, the mean has been subtracted, as it would be better assessed in a discussion about the background, done in the next chapter. The resulting values for the signal have then been divided by the bandwidth of the measurement, which is determined as it was done previously for consistency. This graph shows gaussian shaped noise, as demonstrated by the fitting, both at f_{HC} and f_{OC}, (respectively the modulation frequency of the Helmholtz coil and the optical chopper). This echoes the results in the previous section that showed that non-gaussian distributions occur for noise contributions at frequencies below 80Hz in this set-up. With a similar maximal count, the two histogram have very different standard deviations σ. The ratio between the two is $\sigma_{OC}/\sigma_{HC} = 37.7$, which is in line with the value computed in section 3.1.3 that deduced an estimated value of 40 when comparing the two modulation schemes based on the measured RIN PSD.

The second measurement is done to assess the contribution of the spintronic emitter to the random noise. The results are shown in figure 3.10. By using the same processing method

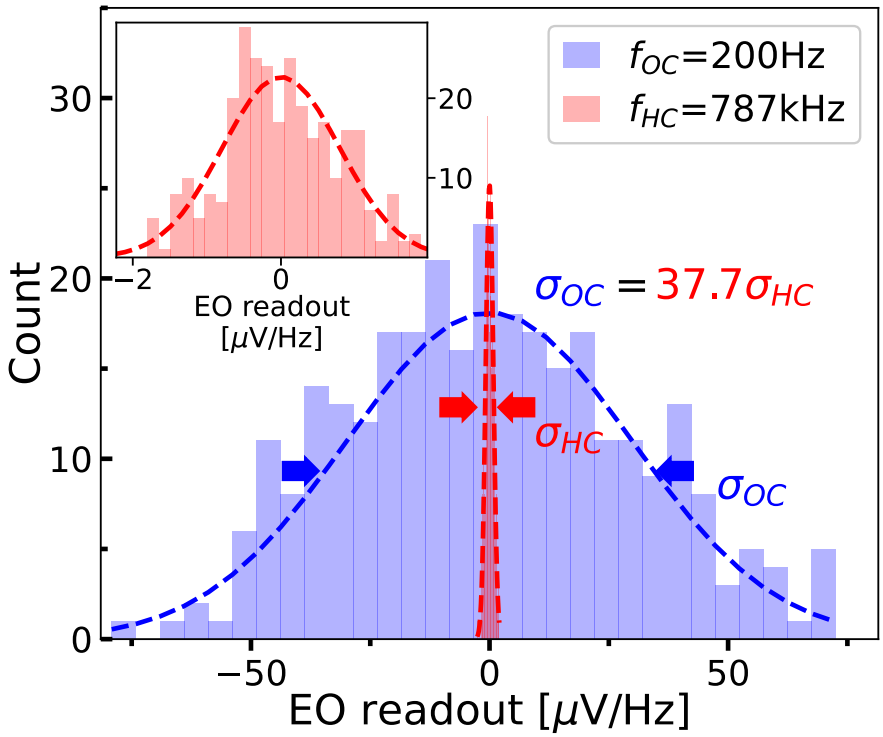

Figure 3.9 Distribution of the electro-optic(EO) readout at negative delay with the spintronic emitter in place. The inset "zooms" in on the distribution for near radio-frequency modulation.

as the first measurement, we show that the value of 37.7 is maintained when the spintronic emitter is taken out of the set-up. This shows that the spintronic emitter does not contribute significantly to the random noise, leaving background noise as the sole noise contribution possible to amplitude noise.

One issue with the two previous measurements is "scalability" : while the results are in line with our expectation, we still need to understand if the noise figure obtained will not scale with and increasing magnetic field. As mentioned in the previous section, data obtained with the chopper is from spintronic emitter under a DC magnetic field bias of 10mT which is the saturation point for the emitter. The factor of 40 between the peak magnetic field when modulated and the saturation point for the spintronic emitter, associated with the linear scaling of the THz field with the magnetic field could then mean a linear scaling of the noise in the set-up and invalidate this result. To prove that the noise doesn't scale with the magnitude of the external magnetic field, histograms are shown in figure 3.11 for the EO readout at f_{HC}. The data as been treated in the same manner as the data used for

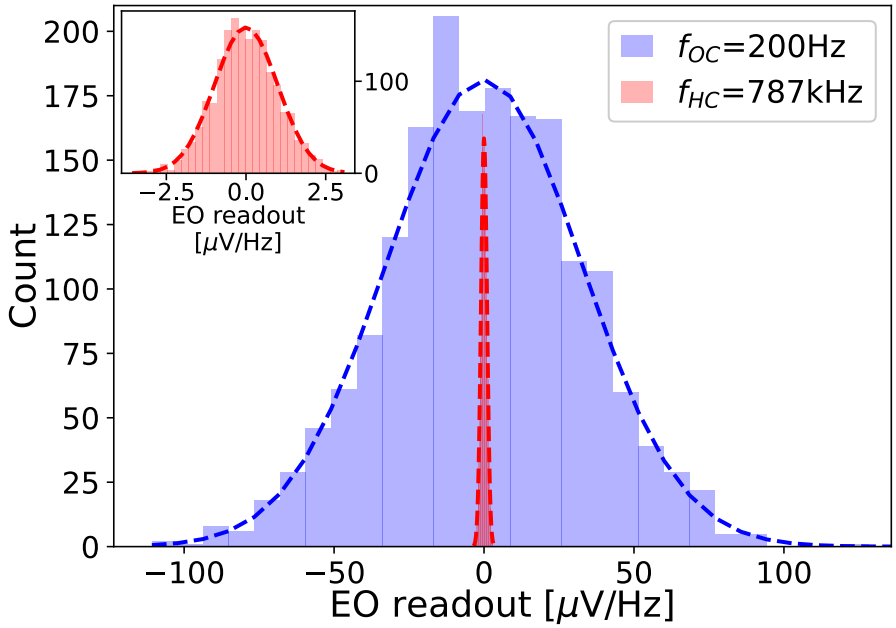

Figure 3.10 Distribution of the electro-optic(EO) readout when the pump arm is blocked. The inset "zooms" in on the distribution for near radio-frequency modulation.

the previous graph. Here we can see that the noise stays at the same level, regardless of the magnetic field produced. This suggests strongly that the noise performance would not deteriorate at 20mT, as it is only dependant on the modulation frequency and independent of the magnetic field.

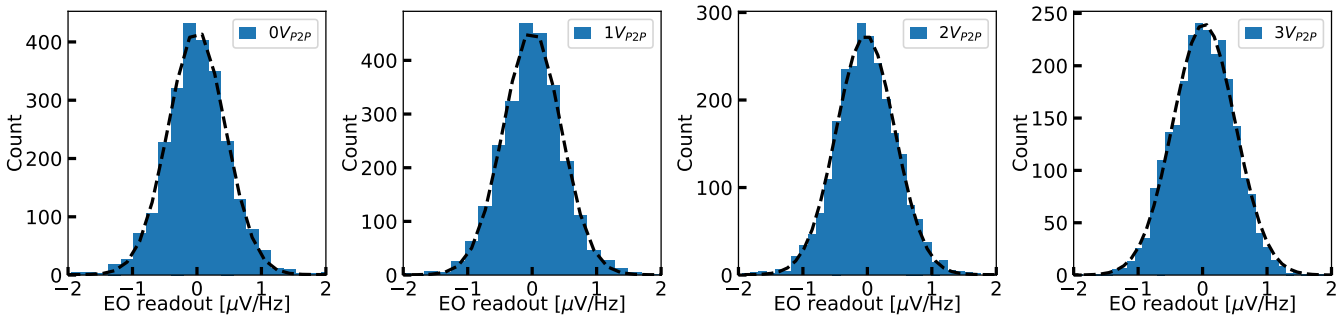

Figure 3.11 Distribution of the electro-optic(EO) readout at negative delay with the spintronic emitter in place, with a modulation frequency of 787kHz. The peak-to-peak voltage indicated is the one used to drive the coil. The dashed lines show a Gaussian fit to the different histograms.

We can conclude that our measurement is shot noise limited. In our case, the sensitivity of the current set-up is 0.794μV/Hz. An improvement of 37.7 is equivalent to 1421 averages of the f_{OC} measurements, which would prove impractical.

CHAPTER 4 HIGH-SENSITIVITY FIELD RESOLVED MEASUREMENTS

In the previous chapter, we showed a functional Helmholtz coil based on a double resonant circuit, and how the achieved modulation speed reduces the measurement noise in the way that we expected it to. In this chapter, we discuss how well the spintronic emitter performs at such modulation frequencies. To do so, we first present the EOS set-up used for the measurements presented in this chapter.

4.1 Electro-optic sampling set-up

As introduced in the previous chapter, the EOS set-up is a pump-probe scheme with the Ti:Sa as it's sole source. The initial horizontal polarization of the laser is flipped by a periscope, giving a vertical polarization, s, perpendicular to the plane of propagation. The pulse is then split into the pump and probe arms by a 96/4 beam-splitter.

Regardless of the THz generation method used, modulation is done in the pump arm. For generation by OR, modulation is handled by an photo-elastic modulator (PEM) (Hinds Intruments PEM-90) followed by an achromatic half-wave (AHWP) (Thorlabs AHWP05M-980) plate for fine tuning of the pump probe. The PEM is effectively a square wave modulator at 167.8kHz, switching between no retardation and a half-wave retardation, oriented at 45°. The pulse then switches between a polarization in the plane of propagation, p, and the s polarization at that frequency. Given that the pulse has been pre-compressed for the dispersion the PEM and AHWP add, these elements remain permanently in the setup. As mentioned in section 3.1.1, the precompression is handled by a pair of chirped mirrors at the output of the laser. The other way of modulating the pump beam is the use of an optical chopper, whose wheel (Thorlabs MC1F10HP) can interrupt the beam at frequencies up to 1000Hz. The added noise from the generated turbulent air and mechanical vibrations limit the usable modulation frequency at 500Hz. The last modulation method, only for the spintronic emitter, is the double resonant Helmholtz coil, previously described, used directly at the position of the generation crystal.

After the AHWP, two mirrors mounted at 90° on a precision linear stage (Physik Instrumente L-511.60DG10) serve as a delay line. It is followed by a protected silver 1-inch diameter focusing right angle off-axis parabolic (OAP) mirror with a focal distance of 2 inches. The generating crystal (GX) is placed at the focus of the OAP mirror to create the THz radiation. The THz radiation is collected by 1.5 inch diameter gold coated right angle OAP with a focal

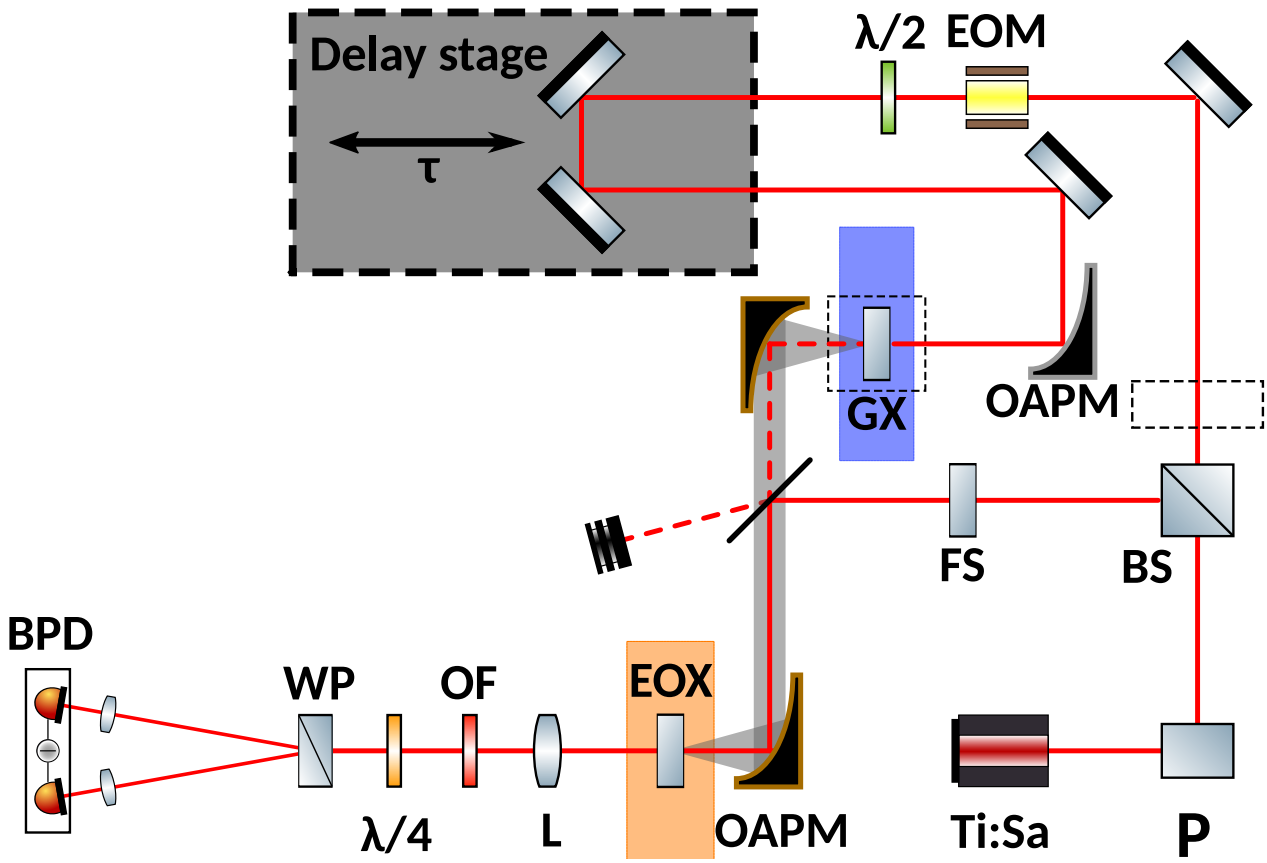

Figure 4.1 Schematic of the electrooptic sampling optical set-up. The two dashed rectangles without filling are the position for the coil (overlapping with GX) or optical chopper (empty rectangle). P: periscope. BS: 96/4 Beamsplitter. FS: 12mm thick Fused Silica. EOM: elasto-optic modulator. OAPM: Off Axis Parabolic Mirror (silver or gold coated). GX: Generation crystal. EOX: Electrooptic crystal. L: lens. OF: Optical filter. WP: Wollaston Prism. BPD: Balanced Photodiode

length of 0.8 inches, placed at 0.8 inches of the focal length of the focusing OAP. This position permits collimation of the collected THz radiation. On the path of the collected beam is a high-resistivity undoped two-side polished silicon wafer. The high resistivity value of 10000Ω.cm ensures high transmission with little distortion to the beam, even for lowest THz frequencies. The 500μm thick wafer is placed at the Brewster angle, rejecting the s polarization of the beam by reflection, and completing the polarization based modulation schemes. Silicon is strongly absorbent at visible to near infrared (NIR) frequencies. As such, the wafer serves also as a filter for the pump beam ensuring that detection channel registers only probe photons. Because the transmission of silicon rises from 10^{-11} to 10^{-5} between 850nm and 925nm, the pump beam is not entirely filtered out. The silicon wafer serves one other crucial purpose: beam recombination between transmitted THz radiation and a

reflected probe pulse.

After the beam splitter, the probe beam goes through a 12mm thick fused silica slab that adds dispersion similar to the dispersion added by the PEM and AHWP in the pump arm. After propagation through this dispersive element, the probe is recombined with the THz radiation by reflection at the Brewster on the silicon wafer.

The recombined beam is focused in the electro-optic crystal (EOX) by OAP mirror identical to the collimating one. After the interaction in the EOX, the beam goes through an ellipsometric set-up, starting with a 25mm focal length collimating lens. The collimated beam is then spectrally filtered. Generally, the beam is filtered using a 890nm shortpass, but the performance of 50nm and 40nm bandpass filters respectively centered at 800nm and 850nm is discussed later. Either of the methods ensures additional suppression of the pump components near the band-edge of the Si wafer beam combiner. The spectral filter is followed by an achromatic quarter wave plate (Thorlabs AQWP10M-980) that changes the linear polarization of the probe to a circular one. After that, an anti-reflection coated Wollaston prism (Thorlabs WP10-B) separates horizontal and vertival polarizations by 20°. Those polarizations are then focused by two small lenses on the two detectors of a switchable gain balanced amplified photodetector (Thorlabs PDB450A). The differential signal is then transferred to the lock-in amplifier (Zurich UHFLI) for demodulation by a shielded SMA-BNC connector to avoid pickup of parasitic fields emitted by the coil.

Parameters for the demodulation, as well as parameters for the displacement of the mechanical stage can be controlled in an unified homemade Python graphical user interface that also serves for saving of the measurement. The whole EOS set-up is kept from dust and other outside perturbations by an custom PVC enclosure, which effectively reduces the environmental noise (e.g. air currents, etc.) in the measurements.

4.2 Low frequency measurements

For the low frequency measurements, we compare the performance of the EOS set-up modulated at f_{OC}=200Hz to what we observe for modulation at f_{HC}=787kHz. In both cases, the EOX is the <110> oriented 500μm thick ZnTe crystal, while the generation is handled by the spintronic emitter. At f_{OC}, the B field is static, with a value higher than the saturation limit of 10mT. At f_{HC}, the peak B field is evaluated to be 254μT. The time constant for the measurement is 100ms. Both measurements shown here where done on the same day for consistency in the comparison. The results are presented in figure 4.2.

From the graph, it is clear that the field emitted at f_{OC} is much stronger than the field

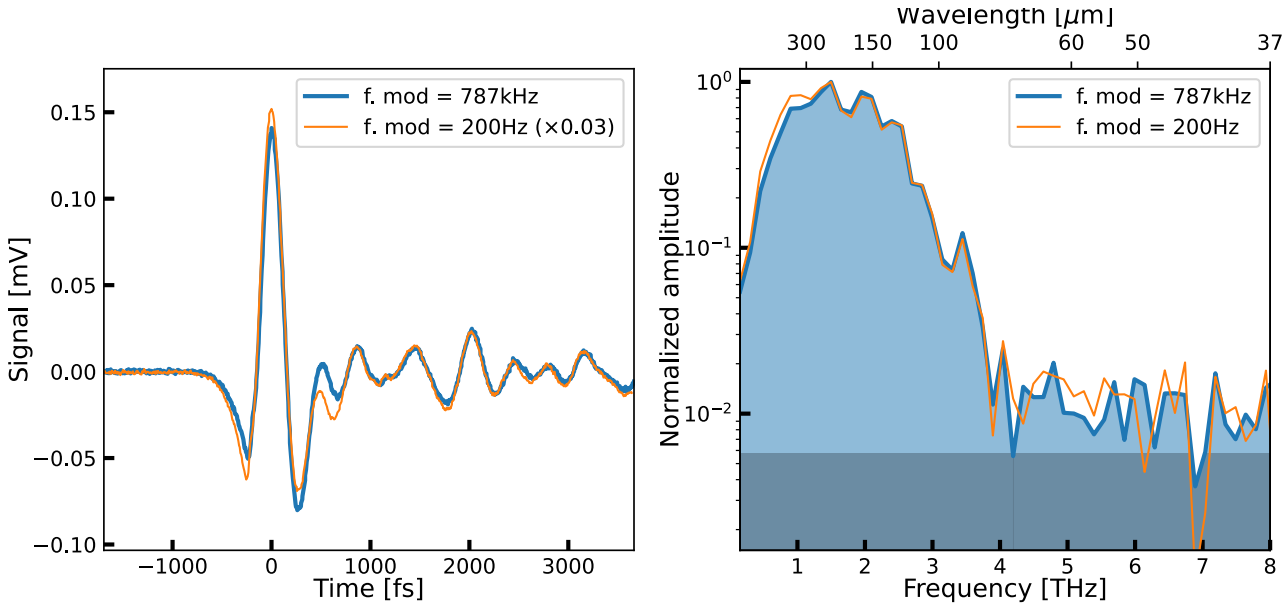

Figure 4.2 Comparison between the spintronic emitted THz, detected through 500μm thick ZnTe at different modulation frequencies. **Left :** Time traces. **Right :** Associated spectra. The dashed area is below the noise floor of the high-frequency modulated spectrum.

emitted at f_{HC}. This is in line with our expectations, as the peak strength of the magnetic field is 39.37 times weaker than the static field and the amplitude of the THz radiation scales with the amplitude of the applied B field. The ratio between the signals respective strength is 31.01 which is a bit smaller than the exact figure quoted above. The difference is strength can be attributed to two contributing factors. The first one being the difficulty to align the center of the coil and the focus of the beam, as the current coil holder does not offer such precision in the positioning. If this perfect overlap were achieved, the second factor might also limit the measured peak-to-peak: when operated at peak input voltage, the coil heats up and its performance decline over periods of time similar to the measurement. While the signal at f_{HC} is slightly under-performing, it demonstrates that the spintronic emitter is able to emit THz radiation with the same time profile as it would with sub-10kHz modulation, which, as far as we are aware, is the first time it is demonstrated. Another important point that the P2P signal comparison drives is the gain in signal provided by sinusoidal modulation in comparison to optical chopping: because the signal oscillate from a positive to a negative peak, a doubling of the measured signal is observed. Going back to equation 2.37 for SNR,

we have:

$$\begin{aligned} \mathrm{SNR_{OC}} &= \frac{S_{OC}}{2\sigma_{OC}\sqrt{\Delta f}} = 173.45\mathrm{Hz}^{-1/2} \\ \mathrm{SNR_{HC}} &= \frac{S_{HC}}{2\sigma_{HC}\sqrt{\Delta f}} = 196.16\mathrm{Hz}^{-1/2} \end{aligned} \tag{4.1}$$

The signal to noise ratio is improved, despite the degraded signal because the noise performance at f_{HC} overcompensates for it.

The similar performance of the spintronic emitter at low frequency is confirmed by the comparison in the frequency domain, obtained by Fourier transform of the time traces shown above. The spectral profiles are the same, as long as we only consider the parts above the noise line and away from the 5.3-6.2 THz Reststrahlen band of ZnTe : the spikes at 6.5, 6.7 and 7.2 THz show how well they are matched.

Below 10THz, the spintronic emitter emits the same spectral profile, whether the modulation frequency is 200Hz or near RF. The modulation at f_{HC} currently brings an advantage in terms of SNR. While it is already better, with a B field 40 times smaller than the saturating field and the linear scaling of the THz radiation with the magnetic field, SNR up to $8000/\mathrm{Hz}^{-1/2}$ is expected in the future.

Impact of spectral filters in ellipsometric set-up: One of the proposed ways to improve the current EOS set was the use of better suited optical filters (OF). With a different OF, the leaking of the pump into the ellipsometric set-up (ESU) would be prevented. An added improvement was a reduction of the input power inside the ESU. With this reduction, an iris would not be needed anymore reducing the possibility of noise originating from beam pointing instability. Here we briefly discuss the impact of different OF on the noise performance of the EOS set-up, but also on the EOS measurement itself. The EOS measurement is the exact same one described in this section, with the OF being changed. The three OF retained for this discussion are the shortpass (SP) filter at 890nm, a 50 nm wide bandpass (BP) filter centered at 800nm, and a 40nm wide BP filter centered at 850nm. The results for the noise performance are shown in table 4.1.

The table shows a decrease of the noise with the size of the accepted spectral range. While it is substantial when going from the the SP to any of the BP, the gain of switching from a 50 to a 40nm BP is minimal. We expect the noise to be linked with the width of the accepted spectral range, which is the case here. On the other hand, the optical power is highest at the central frequency, which has a predictable effect on the noise: the shot noise contribution is lower at higher average power, for similar central frequencies (352THz vs 375THz), according

Table 4.1 Noise performance with different optical filters in the ellipsometric set-up

Filter used	P2P [μV]	σ [μV]	SNR [Hz^{-1}]
SP @ 890nm	120.10	0.44	171.5
50nm BP @ 800nm	67.60	0.29	142.60
40nm BP @ 850	43.66	0.28	95.7

to equation 2.36. Also, the difference in average power for the input means different signal levels, expressed by the peak-to-peak (P2P) in the table. The P2P decreases with the allowed spectral range, as expected. Overall, changing the filter does increase the sensitivity by $\tilde{1}.5$, but the loss of signal is on the same scale, at best. This is also limited by the current filters at our disposal, but a BP filter with a greater acceptance band would be best. The improvement on noise is also accompanied with an qualitative change to the waveform detected, as shown in figure 4.3.

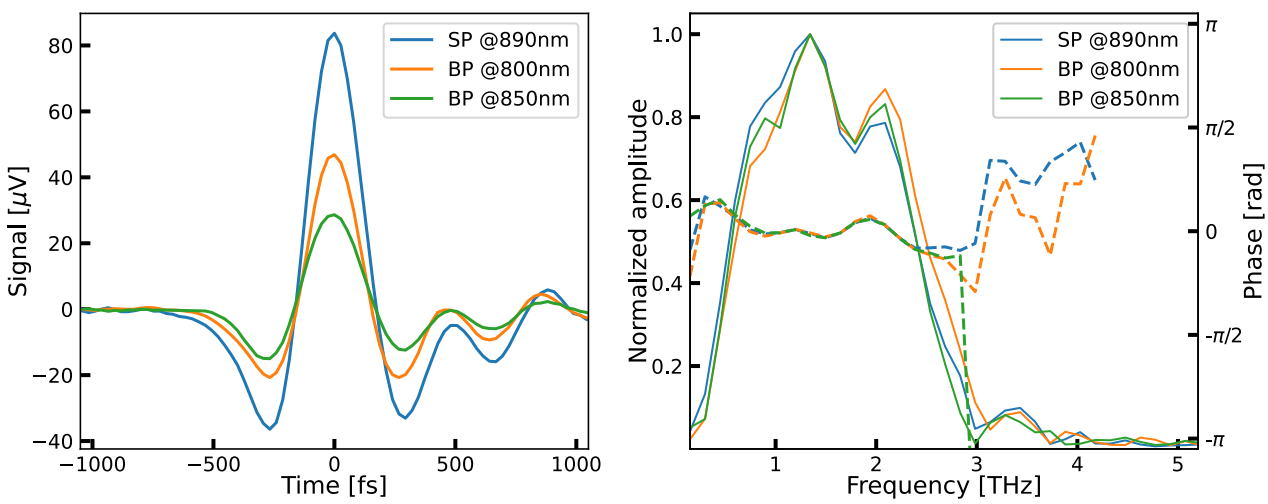

Figure 4.3 Comparison between the spintronic emitted THz, detected through 500μm thick ZnTe, at a modulation frequency of 787kHz for different optical filters in the ellipsometric set-up. **Left :** Time traces. **Right :** Associated spectra and phases.

We see here that the spectra detected is exactly the same for any of the three configurations, as expected. The phase is the same for the three, over the 0-3THz range. Beyond that point, the phase is not properly detected in the case of the 40nm BP, which can be attributed to the low signal level. In the time domain, the traces share the same 'W' shape overall. It is

however clear the main waveform has different symmetry depending on the OF. While the 50nm BP has a perfectly symmetrical shape, characterized by the 1.0004 ratio between the two side dips, the SP and the 40nm BP are asymmetrical, with respective ratios of 1.1005 and 1.2079. These differences are attributed to the difference in the targeted effect: it is established that DFG is the main contributive effect on the high frequency end of the probe, while SFG and DFG are equally contributive in the central part of the probe. It shows that different effects can be easily targeted by different OF in this set-up. It is also an additional motivation to use a wide bandwidth symmetrical BP filter, centered at 800nm to maximise SNR in this set-up.

4.3 High frequency measurements

in the previous section, low frequency THz radiation helped confirm the operation of spintronic emitters at f_{HC}. However, full operation can only be argued if the emitters have the same bandwidth as was measured in the literature. In this section, we do a comparison between THz radiation generated through OR and spintronic emission. For OR, the modulation frequency is f_{PEM}=167.8kHz. f_{HC} is kept the same. Phase-matched detection is done through a z-cut, cleaved and uncoated 30μm thick GaSe EOX, with a phase matching angle of 60°. The time constant of the measurements is set at 100ms and both measurements where done on the same time for the sake of consistent comparison. The results are shown in the figure 4.4.

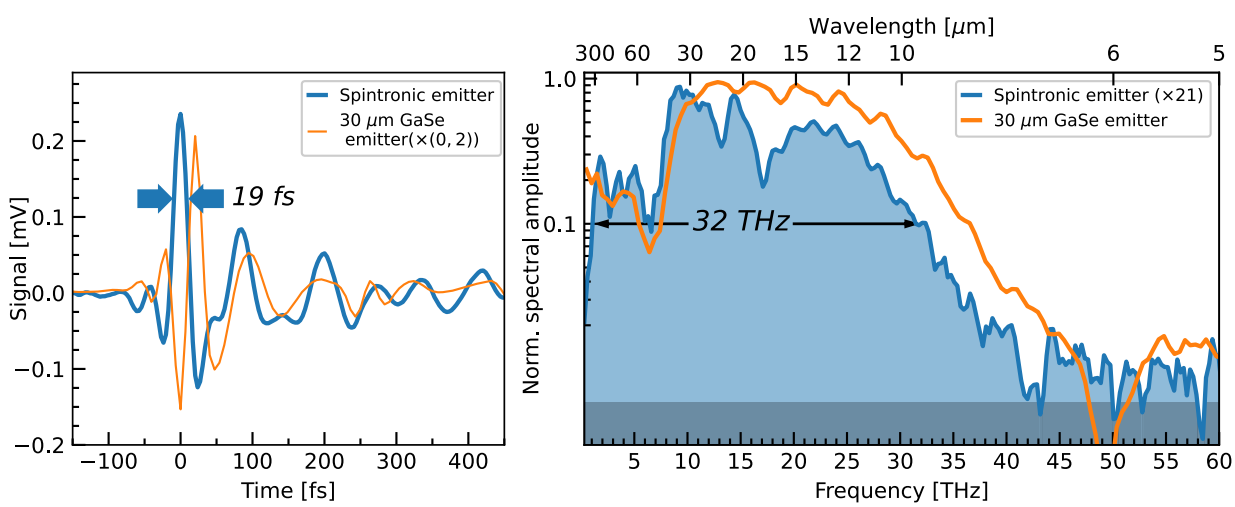

Figure 4.4 Comparison between the spintronic emitted THz, detected through 30μm thick GaSe at different modulation frequencies. **Left :** Time traces. **Right :** Associated spectra. The dashed area is below the noise floor of the high-frequency modulated spectrum.

As was noticed in the previous measurements, direct comparison of the time traces reveal a difference in the strength of the radiated THz pulse. In this case, the OR signal is 4.6 times stronger than the spintronic emission. It is also easily visible that the traces are different in time, which is expected given the different crystals and phenomena used for the generation. The main peak of the spintronic emitter has a duration of 19fs, compared to the 14fs obtained with OR. The four performance values that we previously checked yield :

$$\begin{aligned} \mathrm{SNR_{OR}} &= \frac{S_{OC}}{2\sigma_{OC}\sqrt{\Delta f}} = 91.90\mathrm{Hz}^{-1/2} \\ \mathrm{SNR_{HC}} &= \frac{S_{HC}}{2\sigma_{HC}\sqrt{\Delta f}} = 113.38\mathrm{Hz}^{-1/2} \end{aligned} \tag{4.2}$$

The increase in SNR despite a strong reduction in signal is at first surprising, given the high modulation frequency for the OR. It indicates an increase in noise for the OR, by a factor of 14.91. The background is also higher for the OR, by a factor of 74.33. These figures reinforces the idea that modulation of the pump beam does not discriminate against random noise contributed by other phenomena. Through the modulation of the applied B field, the noise performance stays true to the performance of the Ti:Sa. In the particular case of OR, the added noise and background could be explained by the quality of the phase matching at the GX. While perfect phase matching would ensure strong discrimination against other $\chi^{(2)}$ effects in favor of OR, a small deviation would contribute to these effects while also reducing the signal. In this set-up, the tight focusing at the generation also causes higher order non-linear effects. It can also lead to crystal damage near the focus. On the other hand, the performance of the spintronic emitter is consistent with the results obtained at low THz. It provides outstanding visibility and SNR, which would be crucial for spectroscopy or imaging.

By Fourier transform of the previous results, we obtain the respective spectra for the OR and the spintronic emitter. In the graph on the right in figure 4.4, our direct measurement shows THz components extending beyond 30 THz (10% of peak value at 32THz) in a direct measurement which has not been reported in the literature yet. It is proof that the spintronic emitter is fully functional up to radio frequencies. The performance at low THz was a strong indicator that the emitter would still perform at for broadband emission: the timescales associated with the modulation frequency are greater than the timescales associated with low THz values, and it holds true for values higher than those. The spectra for both the spintronic emitter and the GaSe crystal show dips around 6 to 7THz, which is the Reststrahlen and of the EOX. It serves as an fortuitous mean of calibration in this context. The main dips around 14 and 17THz are also well documented features of the tri-layer emitter used

in our experiment. The smaller features on the spectrum are caused by two known effects. The first is the Fabry-Perot etalon due to the thickness of the GX and EOX. The probe and THz beams go through multiple reflections inside the crystals, which leads to "echoes", or "revivals". The other effect in play is absorption in the air, especially by water vapor known for absorption lines at 200, 55, 25 and 15μm. Comparison between the spectrum produced by the full trace and the spectrum obtained from a trace truncated right after the main peak confirms their impact on the spectrum.

4.3.1 Electron mobility analysis

In spintronic devices, THz emission is produced by accelerating electrons as seen in the theory chapter. As such, information about the mobility of electrons during the THz generating process can be retrieved from THz measurement, which we do in this subsection.

The detected THz in an EOS set-up is a product of the transfer function (see section 2.1.3) and the emitted THz radiation. By changing only the THz source as was done in figure 4.4, the transfer function can be taken out of the measurement. The ratio of two EOS spectra is simply the ratio of the respective THz emissions in the frequency domain. The high frequency measurements shown in this section are prime candidates for this procedure. It is however limited by the presence of the Reststrahlen band where a division by 0 occurs, making it impossible to retrieve any information. It is also not possible to retrieve any worthwhile information in range where the noise is stronger than the signal.

The relative flatness and strength of the detected GaSe spectrum over the 10 to 30THz region makes it a favorable reference over that range. On the other hand, the detected spectrum for the spintronic emitter shows phase flatness extending from the Reststrahlen band up to 35 THz where we see strong oscillations then a discontinuity aroud 45THz, where the signal reaches the noise floor. In regard of these two elements, we consider the ratio obtained to be a good approximation of the emission of the spintronic emitter over this range. Values outside are discarded for being arbitrarily high (around 7THz) or not reliable. The way this was done was by application of a Hanning window to the ratio. This apodization technique also has the advantage of eliminating sidelobes created by the rectangular gate. The results are displayed in figure 4.5. The windowed emission shows a peak at 22THz. The phase is still relatively flat over the considered region.

By inverse Fourier transform of the complex spectrum, the emitted field of the emitter is retrieved in the time domain. Applying a half cycle phase shift in the frequency domain produces the Hilbert transform of the field after an inverse Fourier transform. Combining them yields the envelope, which is shown alongside E(t) and H(E(t))in figure4.5.

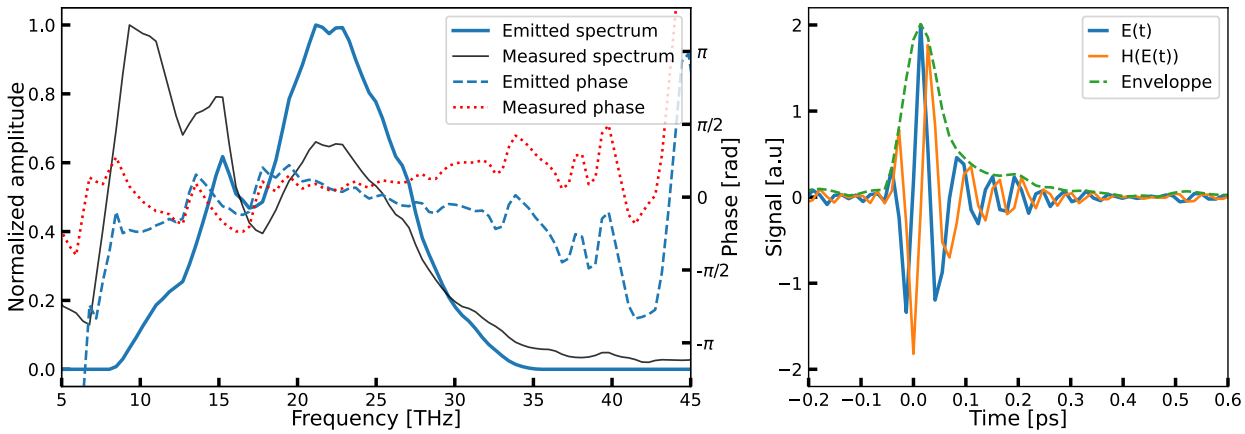

Figure 4.5 THz emission from the spintronic emitter, retrieved through deconvolution. **Left :** The detected spectra and phase are shown with the deconvoluted emission and phase, to which a Hanning window has been applied for apodisation. **Right :** The retrieved field, its Hilbert transform and their envelope in the time domain.

It is already established that E(t) is directly proportional to the spin current in spintronic emitters. As such the exponential decay seen in the envelope of the field is associated with the electron equilibration processes in the sample. In figure4.6, the envelope is fitted with $\Delta\mu_s$, with $\mathbf{\Gamma_{es}^{-1}}$ and the overall amplitude as the only variables. We find that the electron spin equilibration time in this fit is 107fs, which is good agreement with the results in the literature. In this figure, we see good agreement over the first 150fs after the excitation. It is also clear that the fit and the measurement converge toward the same value at large t. Over the 150 to 800fs range, their is a difference with the expected value. It is also the range over which the relaxation is expected to be dominated by electron-phonon relaxation. This discrepancy can be explained by a lower efficiency of this process, which indicates that the crystal is already heated by previous energy deposition in the emitter. The relaxation process is then dominated by the electron-spin equilibration process, by which energy is transferred from the electronic reservoir to the spin reservoir in the three temperature model. The value found for Γ_{es}^{-1} being on the same order of magnitude as the values in the literature is an indication that going from a 2-stack to a 3-stack heterostructure does not affect the relaxation times, which is expected. Another point that this value highlights is the importance of the electron-spin equilibration process : if the spintronic emission processes were reliant on electron-electron processes, the higher time resolution of this current experiment would have resulted in a faster decay. This result is another confirmation that the electron-electron interactions are not the driving force behind ultrafast demagnetization and terahertz spin transport, while

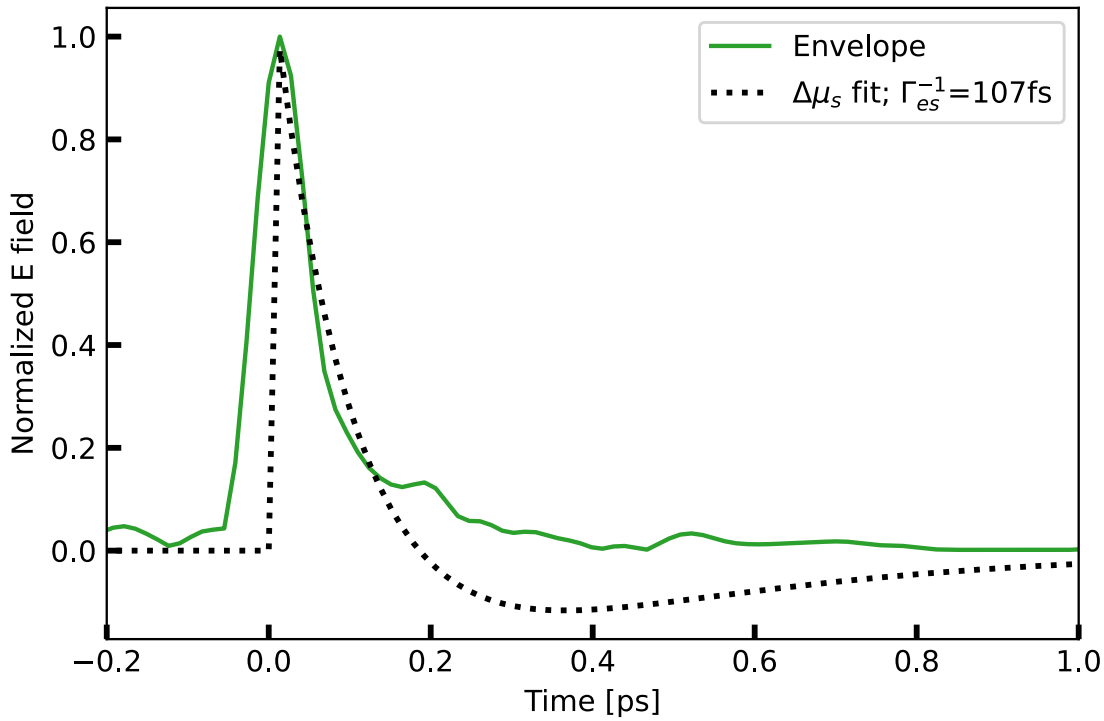

Figure 4.6 Fitting of the tail of the retrieved envelope of the spintronic emission, corrected by the response function of the EOS detector, and the associated lifetime.

electron-spin interactions are.

CHAPTER 5 CONCLUSION

5.1 Summary of current works

The aim of the present project was the improvement of the sensitivity of an electro-optic sampling set-up using a spintronic emitter as its THz source. In order to do so, characterization of the relative intensity noise of the source was carried out in the time and then frequency domain. The power spectral density of the RIN showed that the source became shot-noise limited for frequencies above 160kHz. This informs the range of modulation frequencies for any spectroscopy operating at the standard quantum limit. Compared to the previously used 200Hz modulation of the spintronic emission, an improvement of nearly 40 was measured for the noise performance.

To achieve such high modulation frequencies, advantage was taken of the dependence of the output polarization of the spintronic emitter on the external magnetic field in which the structure is immersed. Sinusoidal switching of the **B** field was done at 787kHz, by use of a Helmholtz coil designed with a double resonant circuit. This prototype produced a peak field of 254μT. The improvement achieved for the noise readings were in line with our calculation before measuring any signal. The demonstrated shot noise sensitivity of THz based time domain spectrometer is first, to the best of our knowledge.

Signal was then measured, at low then high THz frequencies. The low THz measurement was done through 500μm thick ZnTe as the EO crystal, which showed no appreciable differences in the emission profiles of spintronic emitters under two modulation schemes. This shows, in particular, that spins in FM layer can follow externally modulated B-field with great accuracy. The measurement done with the Helmholtz coil reached a higher signal to noise ratio, proving that the lower strength of the **B** field was overcompensated by the shot-noise sensitivity. Similar results where obtained with the high THz measurement, done in a phase matched manner through 30μm thick GaSe as the EO crystal. While the signal to background ratio was systematically better with Helmholtz coil, its level with the optical chopper seems to indicate that the source is electronic and not optical. The spectra detected at low and high THz frequencies for the spintronic emitter demonstrate that, for our purposes, it functions as well at f_{HC} as it did at f_{OC}, contrary to the 100kHz upper limit proposed in the current literature.

The final result presented in this thesis is the analysis of the detected spectrum of the spintronic emitter at high frequencies to extract information about the relaxation processes in-

volved. To the best of our knowledge, the reported results constitute the most wide-band and systematic characterization of the spintronic emitter to date. To this end, our measurement demonstrated a gap-free emission from a spintronic device spanning from less than 1THz to 32THz at 10% level of the amplitude spectral density. This corresponds approximately to a factor of 2 improvement to the highest detected frequency of emission found in the literature. Using 11fs pulses and a pair of 30-μm-thick GaSe crystals as emitter and detector, showed bandwidth of system response in excess of 40THz. This shows that the detected spintronic bandwidth is not system-limited, hence proving the highest frequency detected is an intrinsic limitation of the spintronic THz emission process. Our results directly verify characteristic timescales of the relaxation processes (100fs), attributed here to the electron-spin scattering time within the framework of the three temperature model. These combined results position spintronic devices as promising technology for mid-infrared spectroscopy operating at the standard quantum limit.

5.2 Future work

This project served to establish that magnetic field switching was possible in the current set-up and observe the improvement expected with regards to sensitivity. As is it part of a larger project of setting a high performance spectroscopic system, improvement of the strength of the THz field is crucial. It is an obvious next step, due to the linear dependence of the THz field on the magnetic field, up to saturation. We expect a 40 times improvement in the signal, raising the SNR above 4000Hz$^{-1/2}$ in the broadband case. To do so, another coil has to be built and its design is in current discussions.

A suggestion made to improve SNR in the set-up by the previous member of the laboratory who was predecessor to this work was the use of different optical filters in the ellipsometric set-up [52]. While the filter used have improved the noise performance by 1.5, the low bandwidth of the filters reduced signal, leading to an overall 18% decrease in SNR. The optical noise being contributed by pump photons that are filtered, the noise performance improvement can be recovered in the SNR by using a larger bandpass filter (up to 120nm) filter centered at 800nm. The compounded effect of a saturation-limited magnetic field and the right filter would lead to an SNR higher than 6000Hz$^{-1/2}$, which would be the current limit we would expect without changing the detection crystal, the emitter or the laser set-up.

The high THz bandwidth capabilities of the set-up where demonstrated using 10μm thick GaSe that we unfortunately damaged during the current project. The in-house manufacturing of similar crystal proved difficult and time-consuming, leading to the use of a thicker crystal. The thicker crystal proved thin enough to detect the full bandwidth of the spintronic emitter

down to the 10% line, but it has recently been brought to our attention that 10μm thick GaSe sample are once again commercially available. Such crystals would be better suited for electron mobility analysis and would be useful in characterizing broadband spintronic emitters in the future, as that is one project that the set-up is currently used for.

REFERENCES

[1] M. C. Hoffmann and J. A. Fülöp, "Intense ultrashort terahertz pulses: generation and applications," *Journal of Physics D: Applied Physics*, vol. 44, no. 8, p. 083001, Mar. 2011. [Online]. Available: https://iopscience.iop.org/article/10.1088/0022-3727/44/8/083001

[2] Y. Lee, *Principles of Terahertz Science and Technology*, ser. Lecture Notes in Physics. Springer US, 2009. [Online]. Available: https://books.google.ca/books?id=4ZqkuUURxFcC

[3] X. Zhang and J. Xu, *Introduction to THz Wave Photonics*, ser. SpringerLink : Bücher. Springer US, 2009. [Online]. Available: https://books.google.ca/books?id=ErCzAP7Gi_0C

[4] I. F. Akyildiz, J. M. Jornet, and C. Han, "Terahertz band: Next frontier for wireless communications," *Physical Communication*, vol. 12, pp. 16–32, Sep. 2014. [Online]. Available: https://linkinghub.elsevier.com/retrieve/pii/S1874490714000238

[5] A. Y. Pawar, D. D. Sonawane, K. B. Erande, and D. V. Derle, "Terahertz technology and its applications," *Drug Invention Today*, vol. 5, no. 2, pp. 157–163, Jun. 2013. [Online]. Available: https://linkinghub.elsevier.com/retrieve/pii/S0975761913000264

[6] Y. Cao, K. Nallappan, G. Xu, and M. Skorobogatiy, "Add drop multiplexers for terahertz communications using two-wire waveguide-based plasmonic circuits," *Nature Communications*, vol. 13, no. 1, p. 4090, Jul. 2022. [Online]. Available: https://www.nature.com/articles/s41467-022-31590-z

[7] S. Leinß, T. Kampfrath, K. v.Volkmann, M. Wolf, J. T. Steiner, M. Kira, S. W. Koch, A. Leitenstorfer, and R. Huber, "Terahertz coherent control of optically dark paraexcitons in $cu_2\mathbf{O}$," *Phys. Rev. Lett.*, vol. 101, p. 246401, Dec 2008. [Online]. Available: https://link.aps.org/doi/10.1103/PhysRevLett.101.246401

[8] S. Kumar, "Recent progress in terahertz quantum cascade lasers," *IEEE Journal of Selected Topics in Quantum Electronics*, vol. 17, no. 1, pp. 38–47, 2011.

[9] A. Fisher, Y. Park, M. Lenz, A. Ody, R. Agustsson, T. Hodgetts, A. Murokh, and P. Musumeci, "Single-pass high-efficiency terahertz free-electron laser," *Nature Photonics*, vol. 16, no. 6, pp. 441–447, Jun. 2022. [Online]. Available: https://www.nature.com/articles/s41566-022-00995-z

[10] R. W. Boyd, *Nonlinear Optics, Third Edition*, 3rd ed. USA: Academic Press, Inc., 2008.

[11] B. Saleh and M. Teich, *Fundamentals of Photonics*, ser. Wiley Series in Pure and Applied Optics. Wiley, 2019. [Online]. Available: https://books.google.ca/books?id=rcqKDwAAQBAJ

[12] K. Wynne and J. J. Carey, "An integrated description of terahertz generation through optical rectification, charge transfer, and current surge," *Optics Communications*, vol. 256, no. 4-6, pp. 400–413, Dec. 2005. [Online]. Available: https://linkinghub.elsevier.com/retrieve/pii/S0030401805006565

[13] G. Gallot and D. Grischkowsky, "Electro-optic detection of terahertz radiation," *Journal of the Optical Society of America B*, vol. 16, no. 8, p. 1204, Aug. 1999. [Online]. Available: https://www.osapublishing.org/abstract.cfm?URI=josab-16-8-1204

[14] J. Valdmanis and G. Mourou, "Subpicosecond electrooptic sampling: Principles and applications," *IEEE Journal of Quantum Electronics*, vol. 22, no. 1, pp. 69–78, Jan. 1986. [Online]. Available: http://ieeexplore.ieee.org/document/1072867/

[15] P. Sulzer, K. Oguchi, J. Huster, M. Kizmann, T. L. M. Guedes, A. Liehl, C. Beckh, A. S. Moskalenko, G. Burkard, D. V. Seletskiy, and A. Leitenstorfer, "Determination of the electric field and its Hilbert transform in femtosecond electro-optic sampling," *Physical Review A*, vol. 101, no. 3, p. 033821, Mar. 2020. [Online]. Available: https://link.aps.org/doi/10.1103/PhysRevA.101.033821

[16] C. Kittel, *Introduction to Solid State Physics*. Wiley, 2004. [Online]. Available: https://books.google.ca/books?id=kym4QgAACAAJ

[17] J. Faure, J. Van Tilborg, R. A. Kaindl, and W. P. Leemans, "Modelling Laser-Based Table-Top THz Sources: Optical Rectification, Propagation and Electro-Optic Sampling," *Optical and Quantum Electronics*, vol. 36, no. 8, pp. 681–697, Jun. 2004. [Online]. Available: http://link.springer.com/10.1023/B:OQEL.0000039617.85129.c2

[18] T. Seifert, S. Jaiswal, U. Martens, J. Hannegan, L. Braun, P. Maldonado, F. Freimuth, A. Kronenberg, J. Henrizi, I. Radu, E. Beaurepaire, Y. Mokrousov, P. M. Oppeneer, M. Jourdan, G. Jakob, D. Turchinovich, L. M. Hayden, M. Wolf, M. Münzenberg, M. Kläui, and T. Kampfrath, "Efficient metallic spintronic emitters of ultrabroadband terahertz radiation," *Nature Photonics*, vol. 10, no. 7, pp. 483–488, Jul. 2016. [Online]. Available: http://www.nature.com/articles/nphoton.2016.91

[19] E. Beaurepaire, J.-C. Merle, A. Daunois, and J.-Y. Bigot, "Ultrafast Spin Dynamics in Ferromagnetic Nickel," *Physical Review Letters*, vol. 76, no. 22, pp. 4250–4253, May 1996. [Online]. Available: https://link.aps.org/doi/10.1103/PhysRevLett.76.4250

[20] B. Hillebrands and K. Ounadjela, *Spin dynamics in confined magnetic structures I*. Springer Science & Business Media, 2003, vol. 83.

[21] S. M. Rouzegar, L. Brandt, L. Nádvorník, D. A. Reiss, A. L. Chekhov, O. Gueckstock, C. In, M. Wolf, T. S. Seifert, P. W. Brouwer, G. Woltersdorf, and T. Kampfrath, "Laser-induced terahertz spin transport in magnetic nanostructures arises from the same force as ultrafast demagnetization," p. 23.

[22] B. Koopmans, G. Malinowski, F. Dalla Longa, D. Steiauf, M. Fähnle, T. Roth, M. Cinchetti, and M. Aeschlimann, "Explaining the paradoxical diversity of ultrafast laser-induced demagnetization," *Nature Materials*, vol. 9, no. 3, pp. 259–265, Mar. 2010. [Online]. Available: https://www.nature.com/articles/nmat2593

[23] W. Wu, C. Yaw Ameyaw, M. F. Doty, and M. B. Jungfleisch, "Principles of spintronic THz emitters," *Journal of Applied Physics*, vol. 130, no. 9, p. 091101, Sep. 2021. [Online]. Available: https://pubs.aip.org/aip/jap/article/157914

[24] C. Boudoux, *Fundamentals of Biomedical Optics: From Light Interactions with Cells to Complex Imaging Systems*. Pollux, 2017. [Online]. Available: https://books.google.ca/books?id=8O1UMQAACAAJ

[25] H. Haus, J. Fujimoto, and E. Ippen, "Analytic theory of additive pulse and Kerr lens mode locking," *IEEE Journal of Quantum Electronics*, vol. 28, no. 10, pp. 2086–2096, Oct. 1992. [Online]. Available: http://ieeexplore.ieee.org/document/159519/

[26] G. Agrawal and N. Dutta, *Semiconductor Lasers*. Springer US, 2013. [Online]. Available: https://books.google.ca/books?id=bInTBwAAQBAJ

[27] P. Peebles, *Probability, Random Variables, and Random Signal Principles*, ser. McGraw-Hill series in electrical and computer engineering. McGraw-Hill, 2001. [Online]. Available: https://books.google.ca/books?id=lCxgPwAACAAJ

[28] M. Tahir jamal, A. K. Hansen, M. Tawfieq, P. E. Andersen, and O. B. Jensen, "Influence of pump beam shaping and noise on performance of a direct diode-pumped ultrafast Ti:sapphire laser," *Optics Express*, vol. 28, no. 21, p. 31754, Oct. 2020. [Online]. Available: https://opg.optica.org/abstract.cfm?URI=oe-28-21-31754

[29] R. Paschotta, "Timing jitter and phase noise of mode-locked fiber lasers," *Optics Express*, vol. 18, no. 5, p. 5041, Mar. 2010. [Online]. Available: https://opg.optica.org/oe/abstract.cfm?uri=oe-18-5-5041

[30] "Principles of lock-in detection and the state of the art," p. 10.

[31] "Principles of Boxcar Averaging | Zurich Instruments," Jan. 2022. [Online]. Available: https://www.zhinst.com/en/resources/principles-of-boxcar-averaging

[32] "AC Magnetic Field Generator." [Online]. Available: https://www.accelinstruments.com/Applications/WaveformAmp/Magnetic-Field-Generator.html

[33] T. H. MAIMAN, "Stimulated Optical Radiation in Ruby," *Nature*, vol. 187, no. 4736, pp. 493–494, Aug. 1960. [Online]. Available: https://doi.org/10.1038/187493a0

[34] P. A. Franken, A. E. Hill, C. W. Peters, and G. Weinreich, "Generation of Optical Harmonics," *Physical Review Letters*, vol. 7, no. 4, pp. 118–119, Aug. 1961. [Online]. Available: https://link.aps.org/doi/10.1103/PhysRevLett.7.118

[35] M. Bass, P. A. Franken, J. F. Ward, and G. Weinreich, "Optical Rectification," *Physical Review Letters*, vol. 9, no. 11, pp. 446–448, Dec. 1962. [Online]. Available: https://link.aps.org/doi/10.1103/PhysRevLett.9.446

[36] F. Zernike and P. R. Berman, "Generation of Far Infrared as a Difference Frequency," *Physical Review Letters*, vol. 15, no. 26, pp. 999–1001, Dec. 1965. [Online]. Available: https://link.aps.org/doi/10.1103/PhysRevLett.15.999

[37] J. A. Valdmanis, G. Mourou, and C. W. Gabel, "Picosecond electro-optic sampling system," *Applied Physics Letters*, vol. 41, no. 3, pp. 211–212, Aug. 1982. [Online]. Available: https://pubs.aip.org/aip/apl/article/41/3/211-212/526194

[38] D. H. Auston, K. P. Cheung, J. A. Valdmanis, and D. A. Kleinman, "Cherenkov Radiation from Femtosecond Optical Pulses in Electro-Optic Media," *Physical Review Letters*, vol. 53, no. 16, pp. 1555–1558, Oct. 1984. [Online]. Available: https://link.aps.org/doi/10.1103/PhysRevLett.53.1555

[39] J. M. Chwalek and D. R. Dykaar, "A mixer based electro-optic sampling system for submillivolt signal detection," *Review of Scientific Instruments*, vol. 61, no. 4, pp. 1273–1276, Apr. 1990. [Online]. Available: https://pubs.aip.org/aip/rsi/article/61/4/1273-1276/325615

[40] P. K. Dixon and L. Wu, "Broadband digital lock-in amplifier techniques," *Review of Scientific Instruments*, vol. 60, no. 10, pp. 3329–3336, Oct. 1989. [Online]. Available: https://pubs.aip.org/aip/rsi/article/60/10/3329-3336/320438

[41] A. Nahata, D. H. Auston, T. F. Heinz, and C. Wu, "Coherent detection of freely propagating terahertz radiation by electro-optic sampling," *Applied Physics Letters*, vol. 68, no. 2, pp. 150–152, Jan. 1996. [Online]. Available: https://pubs.aip.org/aip/apl/article/68/2/150-152/65538

[42] Y. Cai, I. Brener, J. Lopata, J. Wynn, L. Pfeiffer, J. B. Stark, Q. Wu, X. C. Zhang, and J. F. Federici, "Coherent terahertz radiation detection: Direct comparison between free-space electro-optic sampling and antenna detection," *Applied Physics Letters*, vol. 73, no. 4, pp. 444–446, Jul. 1998. [Online]. Available: http://aip.scitation.org/doi/10.1063/1.121894

[43] Q. Wu and X.-C. Zhang, "Free-space electro-optics sampling of mid-infrared pulses," *Applied Physics Letters*, vol. 71, no. 10, pp. 1285–1286, Sep. 1997. [Online]. Available: https://pubs.aip.org/aip/apl/article/71/10/1285-1286/67951

[44] "List of Contributors for Volume I," in *Handbook of Optical Constants of Solids*, E. D. Palik, Ed. Burlington: Academic Press, 1997, pp. xv–xvi. [Online]. Available: https://www.sciencedirect.com/science/article/pii/B9780125444156500005

[45] "List of Contributors for Volume II," in *Handbook of Optical Constants of Solids*, E. D. Palik, Ed. Burlington: Academic Press, 1997, pp. xv–xviii. [Online]. Available: https://www.sciencedirect.com/science/article/pii/B9780125444156500017

[46] V. Dmitriev, G. Gurzadyan, and D. Nikogosyan, *Handbook of Nonlinear Optical Crystals*, ser. Springer Series in Optical Sciences. Springer Berlin Heidelberg, 2014. [Online]. Available: https://books.google.ca/books?id=1HL_sgEACAAJ

[47] C. Kübler, R. Huber, and A. Leitenstorfer, "Ultrabroadband terahertz pulses: generation and field-resolved detection," *Semiconductor Science and Technology*, vol. 20, no. 7, pp. S128–S133, Jul. 2005. [Online]. Available: https://iopscience.iop.org/article/10.1088/0268-1242/20/7/002

[48] O. Gueckstock, L. Nádvorník, T. S. Seifert, M. Borchert, G. Jakob, G. Schmidt, G. Woltersdorf, M. Kläui, M. Wolf, and T. Kampfrath, "Modulating the polarization of broadband terahertz pulses from a spintronic emitter at rates

up to 10 kHz," *Optica*, vol. 8, no. 7, p. 1013, Jul. 2021. [Online]. Available: https://opg.optica.org/abstract.cfm?URI=optica-8-7-1013

[49] P. Jepsen, D. Cooke, and M. Koch, "Terahertz spectroscopy and imaging - Modern techniques and applications: THz spectroscopy and imaging - Modern techniques and applications," *Laser & Photonics Reviews*, vol. 5, no. 1, pp. 124–166, Jan. 2011. [Online]. Available: https://onlinelibrary.wiley.com/doi/10.1002/lpor.201000011

[50] S. Kono, M. Tani, and K. Sakai, "Ultrabroadband photoconductive detection: Comparison with free-space electro-optic sampling," *Applied Physics Letters*, vol. 79, no. 7, pp. 898–900, Aug. 2001. [Online]. Available: http://aip.scitation.org/doi/10.1063/1.1394719

[51] Y. C. Shen, P. C. Upadhya, H. E. Beere, E. H. Linfield, A. G. Davies, I. S. Gregory, C. Baker, W. R. Tribe, and M. J. Evans, "Generation and detection of ultrabroadband terahertz radiation using photoconductive emitters and receivers," *Applied Physics Letters*, vol. 85, no. 2, pp. 164–166, Jul. 2004. [Online]. Available: http://aip.scitation.org/doi/10.1063/1.1768313

[52] E. Doiron, "Electric field measurements from terahertz to mid-infrared," Master's thesis, Polytechnique Montréal, 2021. [Online]. Available: https://publications.polymtl.ca/9121/

APPENDIX A MANUFACTURING OF COIL

To make a Helmholtz coil similar to the one produced in the text, the steps to follow are described here. You will need Litz wire, a stand for the coil (our was 3D printed), capacitors (according to your calculations but rated for high voltage), heat shrinks of different sizes, a melting pot, soldering paste, glue rated for the material of your stand and soldering tin.

To make one end of the coil:

- melt tin in melting pot at 540°C
- dip the end of the Litz wire in the soldering paste
- dip the same end in the melting pot until the tin sift through the wires
- twist the same end of the wire

To make the main part of the coil:

- make the first end (follow method described above)
- make the turns around the coil stand. Keep the turns in one layer. Keep the turns tight.
- glue the coil to the stand at the top and at the bottom
- make the other end (follow the method described above)
- put a heat shrink tube over one of the end
- apply heat to the heat shrink until it tightens with the wire
- twist the two ends of the Litz wire together

Now that you have the coil, here is how to integrate it in the double resonant circuit:

- cut two sections of 85cm of Litz wire
- do the ends of these sections (follow method above)
- put the two sections of Litz wire inside a heat shrink and shrink it by heating

- solder one capacitor in parallel of the ends of the coil
- solder the other capacitor on one end of the coil
- solder two ends (one the same side) of the reserved Litz wire with the ends of the coil
- put each junction inside a big heat shrink and shrink it by heating
- put this whole junction inside a bigger heat shrink and shrink it by heating